Ascent and emplacement of buoyant magma bodies in brittle-ductile upper crust

Evgenii E.B. Burov, Claude Jaupart, Laurent Guillou-Frottier

JOURNAL OF GEOPHYSICAL RESEARCH, VOL. 108, NO. B4, 2177, doi:10.1029/2002JB001904, 2003

Ascent and emplacement of buoyant magma bodies in brittle-ductile upper crust

Evgene Burov
Laboratoire de Tectonique UMR 7072, Université de Pierre et Marie Curie, Paris, France

Claude Jaupart
Laboratoire de Dynamique des Systèmes Géologiques, Institut de Physique du Globe de Paris, Paris, France

Laurent Guillou-Frottier
Bureau des Recherches Géologiques et Minières, Orléans, France

Received 29 March 2002; accepted 17 November 2002; published 1 April 2003.

[1] The emplacement of silicic magma bodies in the upper crust may be controlled by density (such that there is no buoyancy to drive further ascent) or temperature (such that surrounding rocks are too cold to deform significantly over geological timescales). Evidence for the latter control is provided by negative gravity anomalies over many granitic plutons. Conditions of diapir ascent and emplacement in this case are studied with a numerical model for deformation and heat transport allowing for ductile, elastic and brittle behavior. A large-strain formulation is used to solve for temperature, stress, strain, and strain rate fields as a function of time for a range of diapir sizes, density contrasts, and background geotherms. The method allows for large viscosity contrasts of more than 6 orders of magnitude and determines the dominant deformation mechanism depending on the local values of temperature, strain, and strain rate. Emplacement depth and final deformation characteristics depend on diapir size and buoyancy. Small diapirs (less than about 5 km in diameter) cannot reach shallow crustal levels and do not involve brittle deformation. In the ductile regime the diapir flattens significantly upon emplacement due to stiff roof rocks and to the free surface above. Late stage deformation proceeds by horizontal spreading, with little upward displacement of roof rocks and is likely to be interpreted as ''ballooning.'' Large diapirs (more than about 5 km in diameter) rapidly rise to shallow depths (1–5 km) and induce brittle faulting in the overlying rocks. In this regime, buoyancy forces may lead to faulting in roof rocks. In this case, late stage ascent proceeds by vertical intrusion of a plug of smaller horizontal dimensions than the main body. Buoyant diapirs keep on rising after solidification, long after the relatively short-lived high-temperature magmatic stage. This may account for some phases of late caldera resurgence in extinct volcanic systems. *INDEX TERMS:* 3210 Mathematical Geophysics: Modeling; 8159 Tectonophysics: Evolution of the Earth: Rheology—crust and lithosphere; 8145 Tectonophysics: Evolution of the Earth: Physics of magma and magma bodies; 8439 Volcanology: Physics and chemistry of magma bodies; 8434 Volcanology: Magma migration; *KEYWORDS:* magma bodies, diapirism, rheology, numerical modeling, plutons, mechanics

Citation: Burov, E., C. Jaupart, and L. Guillou-Frottier, Ascent and emplacement of buoyant magma bodies in brittle-ductile upper crust, *J. Geophys. Res.*, *108*(B4), 2177, doi:10.1029/2002JB001904, 2003.

1. Introduction

[2] The formation of large magma reservoirs and plutons in the upper crust may be achieved by four different mechanisms: diapiric ascent, progressive filling by a continuous supply of magma (ballooning), a succession of discrete diking events and finally tectonically induced magma migration [*Bateman*, 1984, 1985; *Rubin*, 1993; *Miller and Paterson*, 1994, 1999; *Clemens*, 1998; *Petford et al.*, 1993, 2000]. *Clemens* [1998] and *Miller and Paterson* [1999] have recently proposed various field observation criteria for discriminating between these different mechanisms on the basis of experimental and theoretical studies by *Cruden* [1988], *Schmeling et al.* [1988], and *Weinberg and Podladchikov* [1994]. It is difficult to do justice to the complex issues raised by the many authors involved in this controversy and to the large set of field and petrological observations discussed. We only note that available physical models are limited in scope and in the

0148-0227/03/2002JB001904$09.00

number of deformation mechanisms involved, and hence that they may not be sufficiently accurate for comparison with field data. Most theoretical models have ignored brittle behavior and have been developed for nondeformable spherical diapirs [*Schmeling et al.*, 1988; *Mahon et al.*, 1988; *Chéry et al.*, 1991; *Weinberg and Podladchikov*, 1994]. *Bittner and Schmeling* [1995] did allow for diapir deformation, but they ignored brittle behavior and the effect of a free surface at the upper boundary. Furthermore, they focused on dense basaltic diapirs below lower density granitic material. Brittle emplacement mechanisms have been studied in the laboratory using analogue materials. By design, however, such studies ignore thermal aspects and rely on simplified materials that always deform in a single regime (brittle or ductile) regardless of temperature, stress, and strain rate [e.g., *Cruden*, 1988; *Roman-Berdiel et al.*, 1995]). The various simplifications that have been made are likely to affect significantly ascent rates, pluton shapes and emplacement characteristics, as shown by studies on the related problem of salt diapirs [*Poliakov et al.*, 1993a, 1993b].

[3] For the sake of clarity and simplicity, it is useful to restrict the discussion to a few major questions. One question is what dominant mechanism controls the final depth of emplacement. A rising magma body may stall at depth because it has reached rocks with the same density or high mechanical resistance. The latter possibility depends in fact on temperature and on the inability of magma to heat up its surroundings, which in turn depends on the previous history of ascent and cooling. A second question is what determines the ascent rate. Both problems are interrelated, of course, because a rapidly rising magma body retains its heat and hence is able to soften its surroundings. Moreover, the transition between ductile and brittle behavior is largely controlled by local mechanical and thermal conditions. A third question is to determine deformation conditions within and away from a magma body to allow comparison with field observations. These different problems must be addressed simultaneously within a single physical framework. In this paper, we reevaluate the diapir model of pluton emplacement because earlier attempts have relied on rather restrictive assumptions. For example, *Mahon et al.* [1988] and *Schmeling et al.* [1988] have solved for the rise and thermal evolution of a buoyant sphere in a Newtonian fluid. They only considered Newtonian viscous rheology and fixed diapir shape. This probably allows a first handle on the physics of ascent and emplacement, but leads to incorrect predictions of ascent velocity and thermal evolution because the upper crust behaves as a strongly nonlinear strain-softening medium [e.g., *Kohlstedt et al.*, 1995]. *Weinberg and Podladchikov* [1994] solved for the ascent of a hot and buoyant sphere through a non Newtonian power law fluid. They demonstrated that a thin ductile aureole develops at the edges of the diapir, which significantly speeds up ascent. There is field evidence for such an aureole [*Paterson and Fowler*, 1993]. However, *Weinberg and Podladchikov* [1994] also took a fixed diapir shape and did not consider thermal effects. One important aspect has been largely overlooked, the ascent of a buoyant body at high temperature through the uppermost brittle crust. *Chéry et al.* [1991] studied nonlocalized plastic deformation above a buoyant body at shallow depth but were not able to account for faulting and for deformation of the magma body, which had a fixed geometry in their model.

[4] In this paper, we provide a comprehensive description of the various deformation mechanisms involved with the ascent of a magmatic diapir. Three deformation mechanisms are taken into account and solved for simultaneously as a function of the local stress, strain, strain rate and temperature fields. We focus on the thermal aspects of the problem and, for the sake of clarity, we do not consider emplacement in conditions of neutral buoyancy. Thus the diapirs of this study stall below Earth's surface only because they are not able to efficiently deform their surroundings. However, we discuss the neutral buoyancy mechanism and its expected differences with the purely thermal mechanism.

2. Physical Framework

[5] We first discuss the different physical mechanisms involved in order to introduce the important control parameters (Figure 1).

2.1. Ductile Deformation

[6] A simple method to evaluate the effects of cooling on ascent is to compare the characteristic timescales for ascent and for cooling. In a Newtonian fluid, the ascent velocity of a buoyant sphere of radius a is given by Stokes' equation:

$$W_1 = C\frac{1}{3}\frac{\Delta\rho g a^2}{\mu_r}, \tag{1}$$

where μ_r is the average wall rock viscosity and $\Delta\rho$ the density contrast. Constant C depends on the viscosity contrast between the sphere and its surroundings [*Happel and Brenner*, 1983, p. 128]:

$$C = \frac{\mu_r + \mu_d}{\mu_r + (3/2)\mu_d}, \tag{2}$$

where μ_d is the average diapir viscosity. For reasonable values of the various parameters involved, predicted ascent rates are within a range of about 10^{-8}–10^{-10} m s^{-1} [*Clemens*, 1998]. This simple equation shows that ascent is limited by the deformation characteristics of surrounding rocks and depends weakly on the viscosity contrast. Thus even a fully solidified magma chamber can move upward at geologically significant rates if host rocks are at elevated temperatures. Heat transport from the chamber to the surroundings is therefore a key process, as emphasized by the following argument.

[7] Assuming that heat transport through a magma body of radius a is governed by diffusion, the timescale for cooling is

$$\tau_c = \frac{a^2}{\kappa}, \tag{3}$$

where κ stands for thermal diffusivity. Over this time, the magma body has moved over vertical distance H:

$$H \approx W_1\tau_c \approx \frac{\Delta\rho g a^4}{\mu_r \kappa}, \tag{4}$$

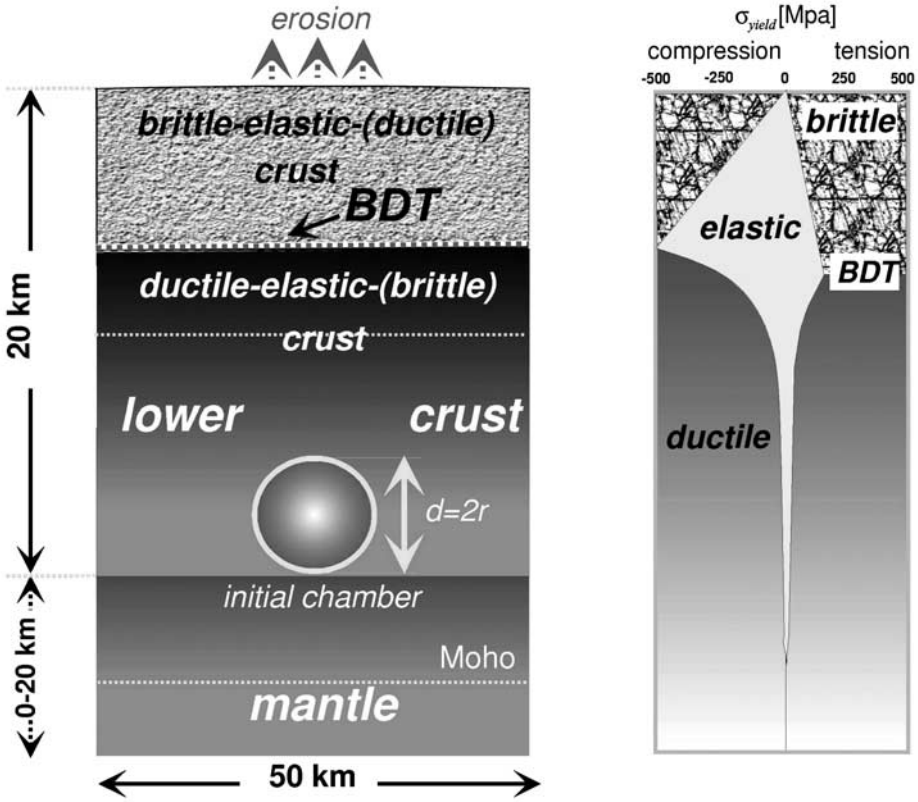

Figure 1. Problem setup. An initially spherical magma reservoir with diameter d and radius r has its base at 20 km depth (left). The upper crust is made of two layers with different densities (Table 2) but a single set of deformation laws. Crustal rheology may be schematically described by a stress envelope on the right, involving ductile, brittle, and elastic deformation mechanisms. Parameters for the stress envelope correspond to a hot geotherm, a background strain rate of 10^{-15} s^{-1}, and dry quartz ductile rheology (Table 2). Note that the brittle domains have less strength in tension than in compression. In reality (and in our numerical experiments), the brittle-ductile transition is a function of the local temperature, pressure and strain rate fields and hence is not imposed a priori. The base of the computational domain at a depth of 20 km deforms such that shear stresses are zero and normal stresses are proportional to the density contrast with the underlying rocks and the local boundary deflection (so-called Winkler restoring force). The upper boundary behaves as a free surface and is subjected to erosion. At the lateral boundaries, the horizontal velocity is set to zero.

which emphasizes the extreme sensitivity to diapir size. For a = 1 km, $\kappa = 10^{-6}$ m^2 s^{-1}, $\mu_r = 10^{18}$ Pa s, which must be regarded as a lower bound and $\Delta\rho$ = 400 kg m^{-3}, which is an upper bound (Table 1), we find that H is about 4 km. This shows that only large diapirs (with radii in excess of 1 km) can be expected to rise through the crust.

[8] This analysis only deals with Newtonian fluids, which is inappropriate for upper crustal rocks. *Weinberg and Podladchikov* [1994] have proposed an approximate solution for power law rheologies such that

$$\dot{\varepsilon} \equiv \frac{\partial \epsilon}{\partial t} = A\sigma^n \exp[-Q/RT], \tag{5}$$

where $\dot{\varepsilon}$ is the strain rate component along the stress axis, A, R, n, Q are material parameters, t is time, and T is temperature. Equation (5) is valid for uniaxial deformation and differential stress, but we follow conventional simplifications [e.g., *Bittner and Schmeling*, 1995] and extend it to three dimensions and deviatoric stress (see Appendix A for details). The characteristic magnitude of deviatoric stress, σ, due to a buoyant sphere is

$$\sigma = \Delta\rho g a. \tag{6}$$

The effective viscosity, μ_{eff}, is given by

$$\mu_{\text{eff}} = \frac{6^{n-1}\exp[Q/RT]}{3^{0.5(n-1)}A[\Delta\rho g a]^{n-1}}, \tag{7}$$

and the corresponding ascent velocity is given by

$$W_2 = \frac{1}{3}\frac{\Delta\rho g a^2}{\mu_{\text{eff}}} \tag{8}$$

Thus $W_2 \propto a^{n+1}$. For crustal rocks, $n \approx 3$ [*Brace and Kohlstedt*, 1980; *Carter and Tsenn*, 1987; *Kohlstedt et al.*, 1995, Table 2], implying that $W_2 \propto a^4$. The dependence on diapir size is therefore much stronger than in the Newtonian case ($W_1 \propto a^2$).

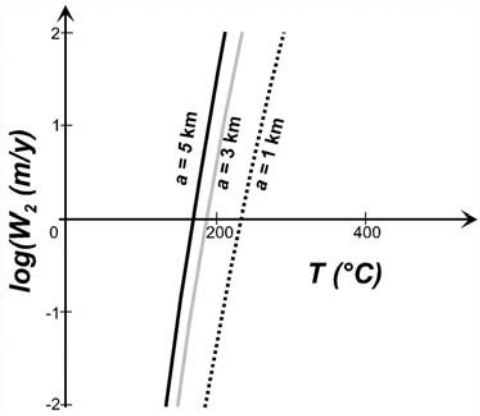

Figure 2. Ascent velocity for nonlinear ductile rheology as a function of temperature (from equation (8)) [*Weinberg and Podladchikov*, 1994]. Parameters are for dry quartz (Table 2). The driving density contrast is taken to be 100 kg m^{-3}.

[9] The ascent velocity is also very sensitive to temperature. Figure 2 shows values of the predicted ascent velocity as a function of temperature for the set of parameters given in Table 2. The key result is that the ascent rate drops to negligible values at temperatures below 200°C, which corresponds to crustal conditions at depths shallower than about 10 km. This rough estimate may be slightly too large because there is field evidence for significant creep deformation in quartz at 5–6 km depth (S. Paterson, personal communication, 2002). Nevertheless, this argument shows that pluton emplacement at shallow crustal levels cannot be achieved in a ductile regime in "normal" thermal conditions. This shows that the diapir size plays a key role because it determines the amount of thermal energy stored in the diapir, and hence the transient temperature field which develops around the diapir as it rises. Interestingly, the critical temperature of 200°C is close to that of the regional brittle-ductile transition for far-field tectonic strain rates [*Carter and Tsenn*, 1987; *Kohlstedt et al.*, 1995].

[10] The above arguments were meant to illustrate a few key physical principles but do not provide accurate results. They are only valid for an undeformable sphere in an infinite homogeneous medium and gloss over the large temperature gradient which develops at the edges of the diapir. A complete solution thus requires numerical techniques.

2.2. Brittle Behavior

[11] The uppermost crust, within 10 km of Earth's surface, remains at temperatures below 200°C if there is no magmatic or plutonic activity. In such conditions, it deforms in elastic and brittle regimes [*Carter and Tsenn*, 1987]. Note that there is an important difference between the regional brittle-ductile transition, which depends on the background temperature field and the far-field tectonic strain rate, and the local transition above a diapir, where temperatures are raised above background values and strain rates are set by local buoyancy forces. We use a simple 2-D model of a thin elastic plate at the top of a ductile medium to demonstrate that a buoyant diapir may generate large extensional stresses in an overlying crustal layer.

[12] At the base of a shallow elastic layer, buoyancy forces due to a diapir are represented by a static line load P_o creating normal stress per unit length p (Figure 3). The flattened diapir has the shape of half cylinder of radius a, and hence

$$P_o = 2\pi\Delta\rho g a^2. \tag{9}$$

The elastic layer is characterized by flexural rigidity D and flexural parameter α:

$$D = \frac{Eh^3}{12(1-\nu^2)}, \tag{10}$$

$$\alpha = \left(\frac{4D}{\Delta\rho_c g}\right)^{1/4}, \tag{11}$$

where E and ν are the Young modulus and Poisson's ratio (see Appendix A for relation with elastic constants of Lamé, λ and G), D is the rigidity, h is the thickness of the brittle layer, and $\Delta\rho_c$ the density contrast between the upper material (air or brittle sedimentary infill) and the ductile substratum. The values adopted for various variables are provided in Table 2. This problem has a well-known solution [*Turcotte and Schubert*, 2002, chapter 3]. The horizontal flexural stress σ_{xx} is largest at the top and base of the brittle layer at the load location where it is equal to σ_m:

$$\max_{x,z}(\sigma_{xx}) = \sigma_m = \frac{3P_o\alpha}{2h^2}. \tag{12}$$

The brittle yield strength, σ_{yield}, or σ_y, is a linear function of confining pressure and hence of depth [*Byerlee*, 1978]:

$$\approx 0.65\rho g z \leq |\,\sigma_y\,| \leq \approx 0.85\rho g z. \tag{13}$$

The condition for brittle failure is

$$|\,\sigma_m\,| > |\,\sigma_y\,| \tag{14}$$

As shown by Figure 3, this condition is met for kilometer-sized bodies at shallow crustal depths. Thus a magma body which has risen to the brittle-ductile transition may continue its ascent in a brittle regime and induce faulting. In such conditions, the behavior of roof rocks may be quite complicated, involving stoping and flexural slip in some circumstances. To study these processes, it is necessary to account for deformation at the upper boundary (Earth's surface).

3. Model Description

[13] The preceding discussion emphasizes that diapir ascent involves several deformation mechanisms and that

Table 1. Density Contrasts Between Magma and Host Rocks According to the Cited Literature

Topic	Density Contrast, kg m^{-3}	Reference
Tabular granites	10–400	*Cruden* [1998]
Molten solidified diapirs	200–400	*Carmichael* [1989]

Table 2. Rheological and Physical Material Parameters and Constants Used in Experiments[a]

Parameter or Constant	Upper Crust	Magma	Lower Crust	Residual Surface Material
ρ, kg m^{-3}	2700	2400–2600	2800	2400
n	3	3	3	3
A, Pa^{-n} s^{-1}	$5. \times 10^{-12}$	$5. \times 10^{-12}$	$5. \times 10^{-12}$	$5. \times 10^{-12}$
Q, J mol^{-1}	$2. \times 10^{5}$	$2. \times 10^{5}$	$2. \times 10^{5}$	$2. \times 10^{5}$
R, J (mol K)$^{-1}$	8.3145	8.3145	8.3145	8.3145
n_g	3.2	–	–	–
A_g, Pa^{-n} s^{-1}	$6. \times 10^{-14.2}$	–	–	–
Q_g, J mol^{-1}	1.44×10^{5}	–	–	–
n_k	1.9	–	–	–
A_k, Pa^{-n} s^{-1}	$1. \times 10^{-15.1}$	–	–	–
Q_k, J mol^{-1}	1.37×10^{5}	–	–	–
λ, Pa	$3. \times 10^{10}$	$3. \times 10^{10}$	$3. \times 10^{10}$	$3. \times 10^{10}$
G, Pa	$3. \times 10^{10}$	$3. \times 10^{10}$	$3. \times 10^{10}$	$3. \times 10^{10}$
C_0 (cohesion), Pa	$1. \times 10^{7}$	$1. \times 10^{7}$	$1. \times 10^{7}$	0
ϕ (friction angle), deg	30	30	30	15
k (thermal conductivity), W m^{-1} K^{-1}	2.5	2.5	2.5	1.5
k_e (coefficient of erosion), m^2 yr^{-1}	500	500	500	500

[a]The assumed flow law parameters A, n, Q for uppermost crustal granites (first 10 km) are chosen to reproduce recent experimental rheologies accounting for strength reduction due to polyphase composition [*Bos and Spiers*, 2002] and strain rate-dependent frictional-ductile flow occurring at low confining pressures [*Chester*, 1995]. The resulting flow law is close to that of weak wet granite A_g, n_g, Q_g used by *Bittner and Schmeling* [1995] and *Brace and Kohlstedt* [1980]. For more consolidated crust below 10 km, we also used a stronger granite rheology from *Kirby and Kronnenberg* [1987] (A_k, n_k, Q_k). The other material parameters come from *Turcotte and Schubert* [2002].

each mechanism operates as a function of local temperature, pressure and strain rate. For such a complex problem, we have sought a numerical solution. The governing equations and the algorithm derived from the ''two-and-a-half''-dimensional (2.5-D) finite element code PAROVOZ [*Poliakov et al.*, 1993a] are described in detail in Appendix A. This dynamic method relies on a large-strain explicit Lagrangian formulation originally developed by *Cundall* [1989] and implemented in the well-known FLAC algorithm produced by ITASCA. Its key features are that it handles true free surface boundary conditions, brittle-elastic-ductile rheology, and that it allows one to follow how material and mechanical interfaces deform. The fully explicit numerical scheme uses adaptative time stepping and hence does not require iterating, which makes it numerically stable even for highly nonlinear rheologies (Appendix A) [*Cundall*, 1989]. The method has many advantages which have been described elsewhere and the price to pay is a very small time step. The code has been tested thoroughly and has been applied to a host of different problems including a number of related problems such as the generation and ascent of salt diapirs, the mechanical stability of shallow magma chambers, passive and active rifting in brittle-elastic-ductile lithosphere as well as Rayleigh-Taylor instabilities in nonlinear media [*Poliakov et al.*, 1993a, 1993b; *Burov and Guillou-Frottier*, 1999; *Guillou-Frottier et al.*, 2000; *Burov and Poliakov*, 2001]. For clarity purposes, we have made a few simplifications whose consequences are easily evaluated and which are discussed briefly at the end of the paper. For example, we do not account for latent heat release by crystallization and ignore density changes due to cooling. Our rationale was to keep the number of variables to a minimum in order to illustrate the main processes and their dependence on an already large number of control parameters.

3.1. Erosion

[14] Our model accounts for surface erosion (Appendix A). As a diapir gets close to the surface, it induces changes of surface topography (e.g., upward flexure or subsidence). Because of large viscosity values and the presence of a free surface above, strain rates are small in the thin roof region. Thus, as it approaches Earth's surface, a diapir slows down and flattens. Erosion rates may vary from 0.1 to 10 mm yr^{-1} and are comparable to surface uplift rates, implying that erosion affects the dynamics of ascent, as shown for salt diapirs by *Poliakov et al.* [1993a, 1993b]. Over the large timescales of our numerical calculations (up to 1 Myr), erosion may remove more than 1 km of material. One effect is that the surface load is selectively reduced (because erosion is faster where topography is high and steep). The other effect is that the mechanically strong brittle layer gets thinned locally [*Burov and Poliakov*, 2001]. One key consequence is the dramatic reduction of ''mushrooming'' at the top of the diapir, which may lead to a final body in the form of an almost vertical tube [*Poliakov et al.*, 1993b].

[15] We have used the conventional linear diffusion equation for erosion (see Appendix A) with a scale-dependent diffusion coefficient of 500 m^2 yr^{-1}, as suggested by experiments and field data [*Avouac and Burov*, 1996]. Avouac and Burov have shown that due to mechanical equilibrium conditions and inherent properties of the diffusion equation (Appendix A), the erosion rate gets automatically tuned to the uplift rate so that the value of the diffusion coefficient need not be known to a high degree of accuracy. In the examples of this paper, a typical length scale is about 10 km, implying that a characteristic value of the erosion rate is 5 mm yr^{-1}, which is comparable to geological values. As will be shown later, this is of the same order of magnitude as the ascent velocities.

3.2. Model Parameters and Initial Conditions

3.2.1. Model Geometry

[16] Calculations were carried out over a 50-km-wide computational domain over heights of 20 or 40 km, with 200 $\times$ 80 or 400 $\times$ 80 elements (see Figure 1 for general setup). The size of the domain was selected as a compromise between minimizing computation time, minimizing

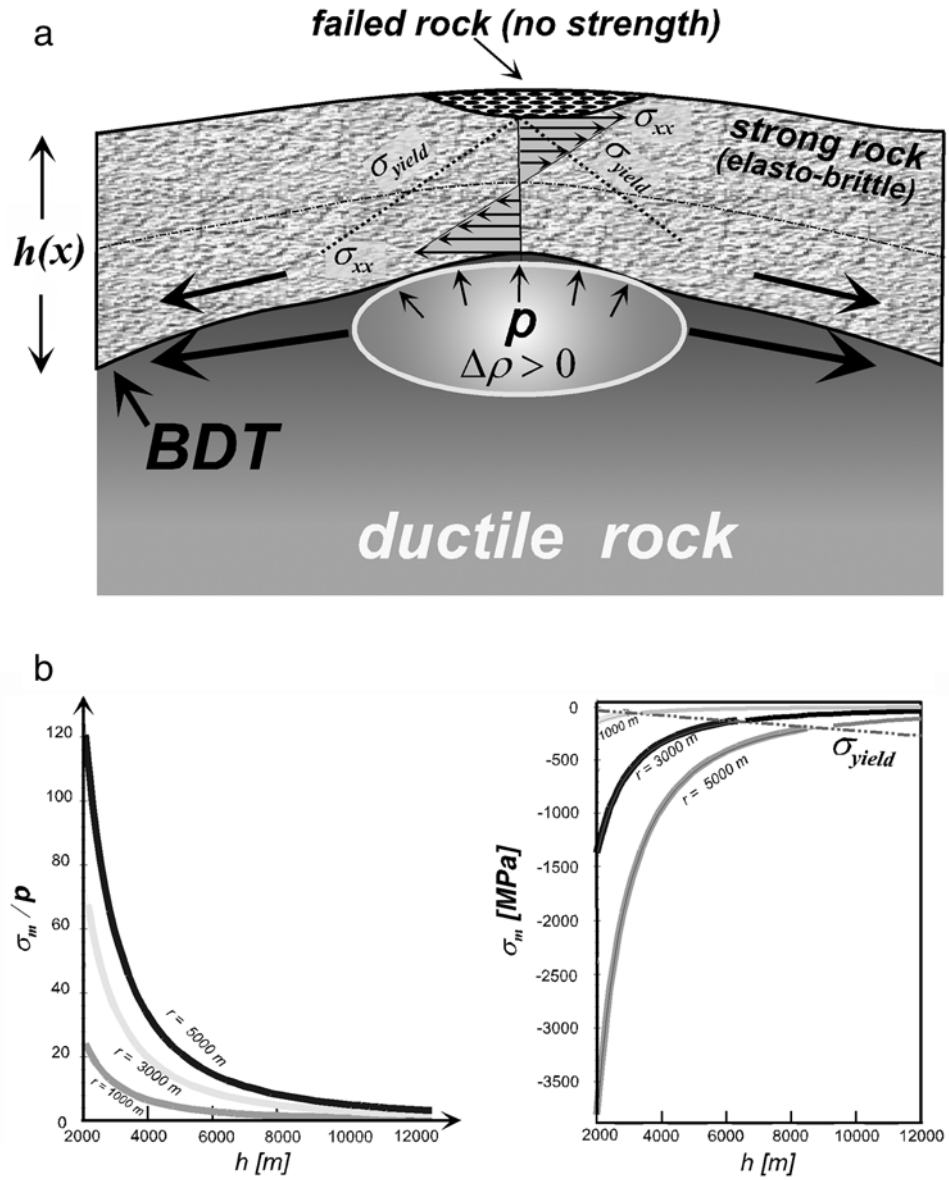

Figure 3. (a) Diagram for a simple model of brittle crustal behavior in a layer overlying a buoyant diapir. Buoyancy forces induce flexure and tension in the layer, which may exceed the local brittle strength σ_y, or σ_{yield}. Variables are described in the Table 2. (b) Strongly simplified analytical estimates of stresses induced by a buoyant diapir in brittle upper crust. Calculations are shown for different diapir sizes *r*. (left) Maximum elastic stress ($\max(\sigma_{xx}) = \sigma_m$, see equation (12)) scaled to buoyancy load per unit length *p*, as a function of brittle layer thickness *h*. (right) Maximum elastic flexural stress σ_m as a function of brittle layer thickness *h* (σ_{xx} takes equal maximal absolute values at the layer interfaces $z = 0$ (extension) and $z = h$ (compression). Since the brittle strength is zero at $z = 0$ and linearly grows with depth (equation (13)), the maximal possible extensional stress in a real brittle-elastic plate equals σ_{yield} at some depth *z* greater than 0 and smaller than *h*/2, at small plate curvature. This maximal depth streams to $z = h$ at very high curvatures (increasing load) because in this case the neutral plane may be shifted from $z = h/2$ to almost $z = h$ (the exact expression for maximal stress in brittle-elastic plate is bulky and is given by *Burov and Diament* [1992]). Dashed line shows the brittle strength limit σ_{yield} (σ_y in the text) at $z = h$, which is absolute stress limit in the layer.

edge effects and minimal resolution needed to localize brittle shear bands.

[17] We have not considered initial stages of diapir formation, by, for example, Rayleigh-Taylor instability of a buoyant layer. One reason is that the wavelength and size of the diapir depend on the dimensions and rheological contrasts involved, including that of the substratum beneath the buoyant layer. This would not allow a simple parameterization of diapir size. Another reason is that one would need to solve for the behavior of a domain of rather large horizontal dimensions to capture the dominant wavelength of instability. We therefore restrict ourselves to a fully

developed diapir that has detached from its source. It may be shown that, in an infinite medium, a finite body rising in a laminar regime must keep a spherical shape [*Batchelor*, 1967, p. 238]. In geological conditions, diapir ascent occurs at small Reynolds numbers and thus in the laminar regime, and hence we have started all calculations with a circular body. This has the added advantage of allowing comparisons with previous studies [*Cruden*, 1988]; *Mahon et al.*, 1998]; *Schmeling et al.*, 1988; *Weinberg and Podladchikov*, 1994].

3.2.2. Rheology

[18] In most calculations, the continental crust is attributed a single brittle-elastic-ductile rheology but is layered in density. Specifying constitutive ductile flow laws for upper crustal rocks, which contain water and are characterized by large variations of mineralogy and texture, is a difficult task [e.g., *Kohlstedt et al.*, 1995].

[19] Values for quartzite have been used widely because of a lack of data on other rock types, but this choice is questionable [*Brace and Kohlstedt*, 1980]. A recent review by *Kohlstedt et al.* [1995] suggests that quartzite and granite rheologies significantly overestimate upper crustal strength especially at small confining pressures (<10 km depth). Laboratory measurements and direct observations suggest that the strength of uppermost crustal rocks is at most 50–200 MPa [e.g., *Kohlstedt et al.*, 1995; *Chester*, 1995; *Bills et al.*, 1994] instead of the 500–700 MPa value for quartzite [*Kirby and Kronenberg*, 1987]. *Bos and Spiers* [2002] have argued that very weak phases such as micas or albite provide a good approximation. It should be also noted that for the rather differential stresses of our problem (<1–5 MPa, equation (5)), diffusion creep prevails, resulting in viscosity values that are much smaller than for dislocation creep.

[20] For these reasons, we have selected a flow law that falls in between *Chester*'s [1995] lower bound and common estimates for wet granite (Table 2). We have also tested harder granite rheologies for comparison (Appendix A and Table 2). Finally, we have used conventional elastic and brittle parameters (Table 2). We have used the same flow laws for both the magma body and surrounding crust, implying that rheological contrasts between the two media are due to temperature differences only.

3.2.3. Viscosity Range

[21] Most available numerical schemes have difficulties with viscosity contrasts in excess of 10^5, which may generate problems for a realistic model. In this study, there is no such limitation. However, numerical stability requires that the time step is kept below the propagation time of elastic waves and below the Maxwell relaxation time for the smallest element [e.g., *Cundall*, 1989]. Accounting for very small viscosity values thus considerably increases the computation time. Here, we are not interested in short timescale and small length-scale motions within the molten magma body (for example, convective currents). For the bulk deformation pattern around the rising and deforming body, it is sufficient to impose an internal viscosity 2–3 orders of magnitude smaller than the host rock viscosity [see, e.g., *Bittner and Schmeling*, 1995]. Smaller viscosity values would not affect the results, as shown, for example, by equation (1). For these reasons, we introduced a lower viscosity cutoff. We tested values in the range of 10^{15} Pa s to 10^{19} Pa s. Crustal viscosity values for our background geotherms do not fall below 10^{19}–10^{20} Pa s [e.g., *Burov and Cloetingh*, 1997], and we found no significant differences between calculations with viscosity cutoffs $<10^{18}$ Pa s. All calculations reported here were made with a safe cutoff value of 5×10^{16} Pa. Note that this only affects the internal circulation within the magma body and that the external medium behaves as predicted by the flow law for all temperatures. In this study, the viscosity contrast between hottest material at the base and coldest material at the brittle transition was as high as 10^{11}, which ensures that diapir ascent is handled in a correct way.

3.2.4. Density

[22] We consider two crustal layers with densities ρ_1 = 2700 kg m^{-3} and ρ_2 = 2800 kg m^{-3}. The diapir is characterized by density ρ_d and initial temperature contrast ΔT. The density contrast is defined to be $\Delta\rho = \rho_1 - \rho_d$. It is clear that some silicic magmas eventually settle at a neutral buoyancy level, but this is not necessarily true in all cases.

[23] Density values for rhyolites and granites, corresponding to molten and solidified silicic material, may be as low as 2300 kg m^{-3} and 2500 kg m^{-3}, respectively [*Carmichael*, 1989] (Table 1). Granites and diorites have densities of 2660 ± 60 kg m^{-3} and 2860 ± 120 kg m^{-3}, respectively. Gneisses have densities of 2700 ± 90 kg m^{-3} [*Judd and Shakoor*, 1981]. Thus silicic magmas may clearly be significantly less dense that upper crustal rocks. Adding the effect of temperature (at least 50 kg m^{-3}), it appears that values of 100–200 kg m^{-3} for the density contrast are quite representative. The largest value considered in this paper (400 kg m^{-3}) is an upper bound but it is not unrealistic: some gneisses have densities of up to 3150 kg m^{-3}.

3.2.5. Temperature Structure

[24] We have used an initial diapir temperature contrast of ΔT = 500°C. Instead of varying both the temperature contrast and the background geotherm, we kept ΔT at the same value and changed the background geotherm. The resulting initial magma temperature at 20 km depth was T_d = 800°C–1000°C. These values are appropriate for most silicic magmas. Higher temperatures (e.g., for basalts) would enhance local heating of host rocks around the diapir with predictable results.

3.2.6. Boundary and Initial Conditions

[25] The upper boundary behaves as a free surface and may be subjected to erosion (Appendix A and Table 2). At the lower boundary, shear stresses are kept to zero and normal stresses are calculated as a function of basal deflection topography using the isostatic approximation (corresponding to so-called "Winkler" restoring forces). At the lateral boundaries, velocities are zero and pressures are equal to lithostatic values.

[26] In order to visualize bulk deformation, the uppermost crustal layer have been split into two different units identified by different colors in the figures. We took two different initial geotherms corresponding to "cold" and "hot" lithosphere as appropriate for cratons and tectonically active regions respectively. These two geotherms correspond to different values of the mantle heat flow and the same average heat production, and can be characterized by the temperature at 20 km depth, or by the temperature (and strain rate) controlled depth of the regional brittle-ductile transition. In these two cases, in the absence of local thermal perturbations, the regional brittle-ductile transition roughly follows the 300°C isotherm and lies at depths of about 10 and 20 km,

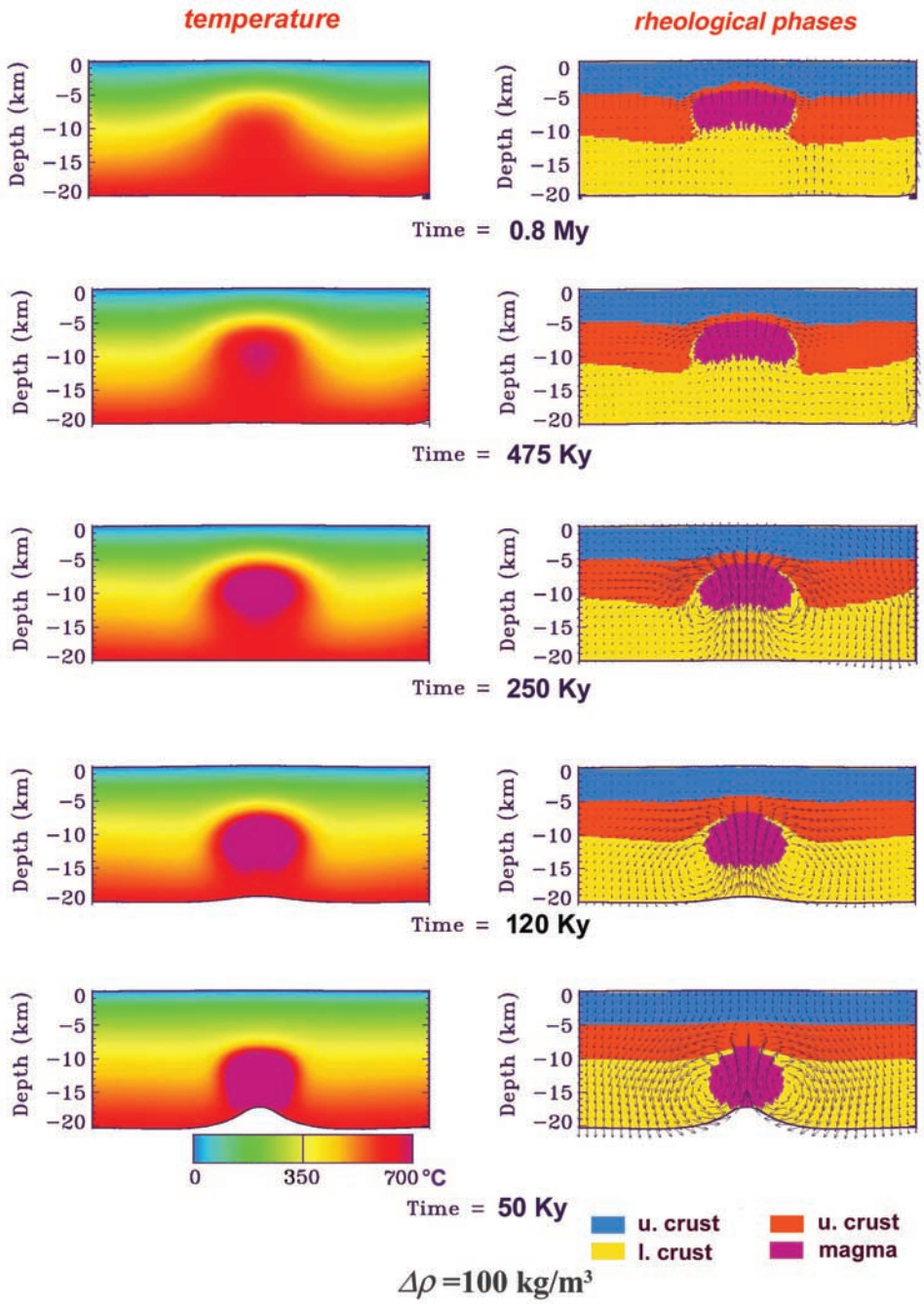

Figure 4. Calculations for a diapir with diameter d = 10 km and density contrast $\Delta\rho$ = 100 kg m^{-3}, in a hot background geotherm. The values of all parameters are given in Table 2. (left) Temperature field. (right) Bulk deformation pattern with arrows for local velocity vectors. To better trace crustal deformation, the upper crustal layer is split into two physically identical units shown with two different colors.

respectively. We shall show that ascent rates are weakly affected by the background geotherm because they depend on the local temperature field in the vicinity of the diapir.

[27] At time t = 0, an initially spherical body is emplaced at 20 km depth and is allowed to rise. Model parameters were systematically varied in order to derive some clear understanding of the effects involved. We have varied the chamber dimensions, the initial temperature contrast (via variation of the background geotherm) and the compositional (chemical) density contrast between the magma body and surrounding crust.

4. Dynamics of Ascent Through Brittle-Ductile Crust

4.1. A Reference Calculation

[28] We compare results of numerical experiments for various initial magma chamber sizes, background geo-

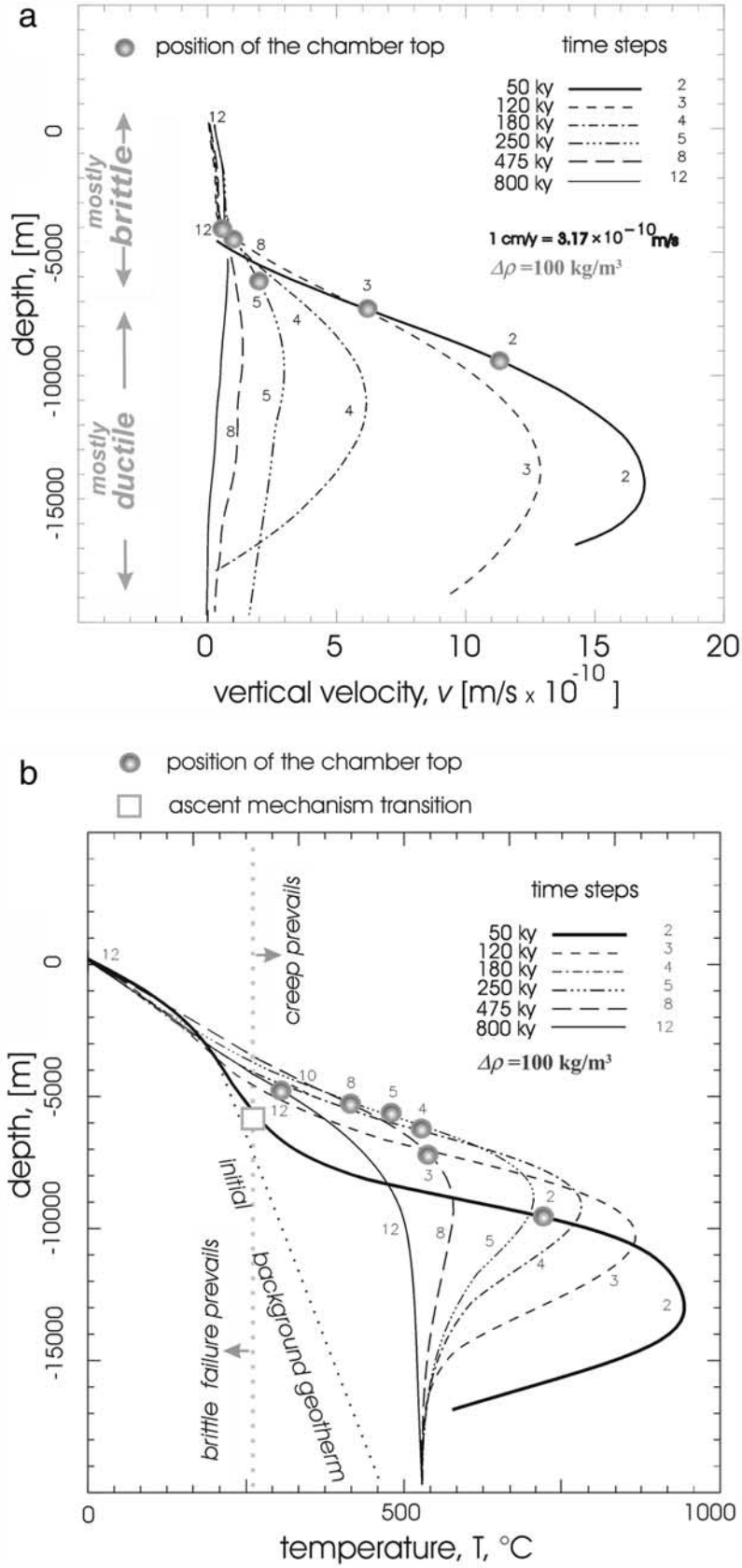

Figure 5. (a) Profiles of vertical velocity through the center of the diapir as a function of depth for the model of Figure 4. Solid circles indicate the top of the diapir. (b) Vertical temperature profiles through the diapir center as a function of depth for the model of Figure 4. Square indicates that the local brittle strength has been exceeded.

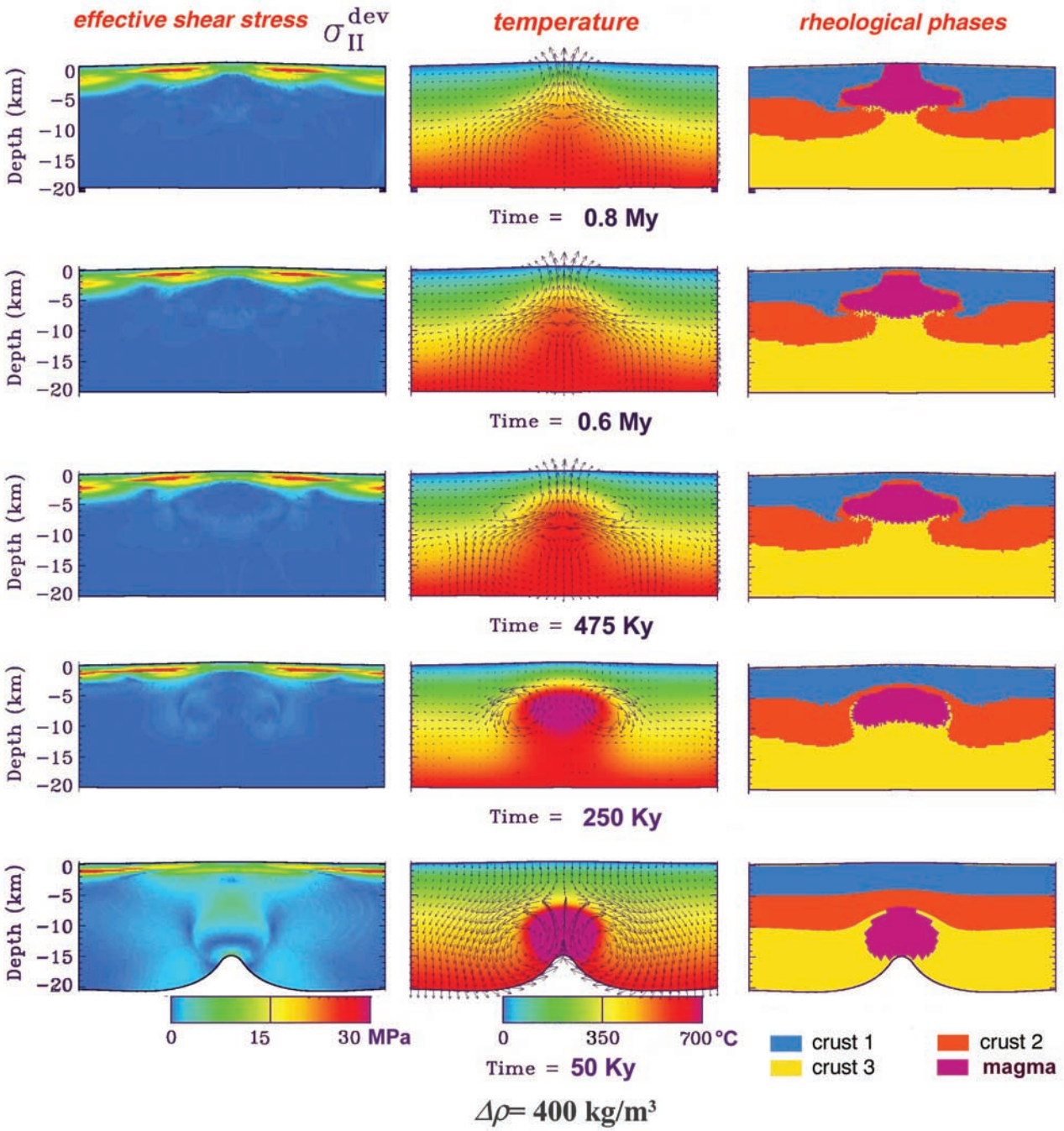

Figure 6. Calculations for a diapir with diameter d = 10 km and a large density contrast $\Delta\rho$ = 400 kg m^{-3}, in a hot background geotherm. The values of all parameters are given in Table 2. (left) Effective shear stress (second stress invariant, see Appendix A). Note that large stresses develop near the surface, which lead to faulting. (middle) Temperature and velocity field. The diapir continues to rise when it has cooled below magmatic temperatures. (right) Bulk deformation pattern. To better trace crustal deformation, the upper crustal layer is split into two units with identic properties but marked with two different colors. Brittle faulting allows a plug of diapir material to reach the surface. Note the changes of dip for the diapir boundary and the poorly developed "root" at the base. The initial layered crustal structure is almost completely restored beneath the diapir.

therms, and density contrasts. We describe one reference calculation in detail, with an initial diameter d of 10 km and a moderate density anomaly ($\Delta\rho$ = 100 kg m^{-3}) in hot lithosphere. This corresponds to high efficiency for ascent: the large volume implies both a large buoyancy force and a large initial heat content, and surroundings are hot. Figure 4 shows the temperature distribution and bulk deformation at several different times. For such a magma

chamber, one may expect the thermal anomaly to dissipate in time $\tau \approx d^2/\kappa \approx 0.8$ Myr (with $\kappa = 4 \times 10^{-6}$ m^2 s^{-1}). It is instructive to compare the bulk deformation map, which shows how material boundaries have moved and deformed, and the thermal field. The initially spherical body starts deforming significantly when it is at a depth about equal to its diameter (i.e., 10 km). At t = 250 kyr, the rising body has been flattened and rises at a reduced rate. The temperature field is characterized by a mushroom-shaped anomaly with a hot tail beneath the reservoir due to the heated ascent path. At later times, the ascent velocity is small and heat diffusion acts to smooth out the thermal anomaly (Figures 4 and 5). Another effect is that erosion becomes significant, i.e., is able to erode away material at a velocity which is comparable to the uplift velocity of the upper surface. The body stalls at a depth of ~5 km, i.e., close to the brittle-ductile transition (Figure 5). The moderate density anomaly is not sufficient to activate important faulting and there is no surface expression save for some moderate uplift.

[29] The diapir has entrained material from the lower crustal layer into the upper layer (this is shown by the thin yellow sliver which lines up the diapir margins in Figure 4). Another feature is that the velocity field is characterized by two large eddies which involve material from both the diapir interior and its surroundings. This internal circulation has been used to define the petrological signature of diapiric ascent, a characteristic zonation such that the core facies is repeated in marginal units [e.g., *Schmeling et al.*, 1988; *Molyneux and Hutton*, 2000]. One should note, however, that this may get overprinted by late stage deformation with completely different characteristics.

[30] The diapir continues to rise even when it has cooled significantly, and the latest stages of ascent are characterized by flattening deformation, such that material from the lower end of the diapir continues to rise while the top barely moves. The edges of the diapir therefore experience a large component of horizontal motion, and deformation markers in country rock record some expansion. This brings in the ancient debate about ballooning [e.g., *Molyneux and Hutton*, 2000], which we discuss in section 5.4.

4.2. Brittle Deformation

[31] Brittle deformation gets activated when the differential stress exceeds the pressure (i.e., depth) dependent yield strength limit. As shown in equation (13), this stress is largely conditioned by the buoyancy force exerted by the magma body, which increases with the body size and its density contrast. The effect of brittle behavior can be illustrated by comparing the previous calculation with two different ones. In one of those, we take the same initial body size (d_o = 10 km) but use a higher density contrast ($\Delta\rho$ = 400 kg m^{-3}). The second one is identical but has no plastic(brittle) behavior, i.e., only account for viscous (ductile) and elastic deformation.

[32] We first consider a larger density anomaly ($\Delta\rho$ = 400 kg m^{-3}). The initial stages are almost identical, with in particular similar thermal evolutions (Figure 6). However, at large density contrast, large forces are exerted on the brittle upper crust and activate faulting. This completely modifies the reservoir shape, which intrudes the surroundings along bounding faults (Figure 7). Similar deformation

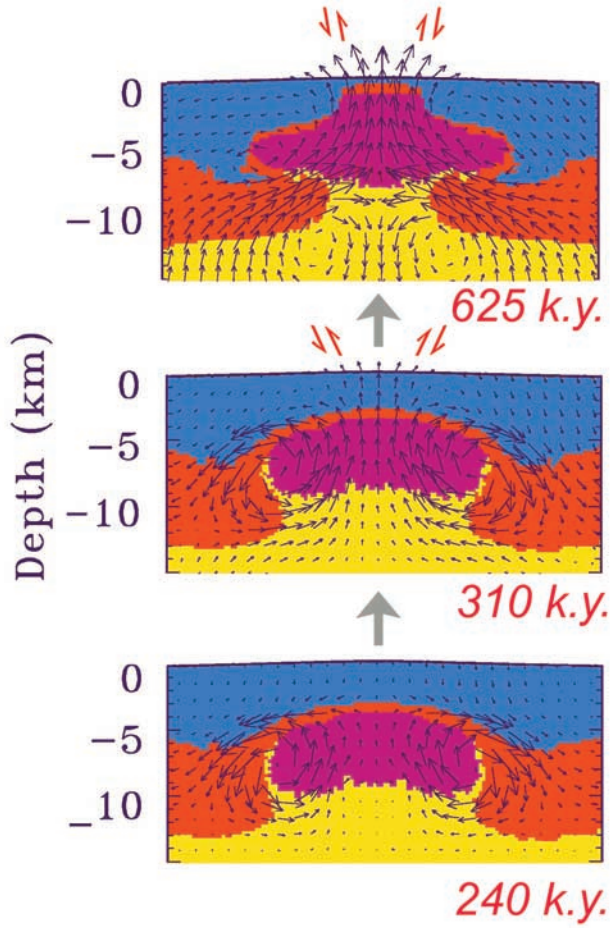

Figure 7a. Close-up of the deformation pattern and velocity field for the diapir of Figure 6. Note that the internal circulation changes as the diapir breaks through the roof zone in brittle fashion.

patterns have been found in laboratory experiments involving brittle material [*Roman-Berdiel et al.*, 1995]. A key fact is that the intrusion process occurs when the reservoir is cold, implying strong mechanical coupling between reservoir and surroundings. In this case, there is less internal circulation within the diapir (Figure 7). Values of ascent velocity and temperatures are given in Figure 8. Brittle deformation clearly affects the final pluton shape. It also affects the entrainment characteristics. The close-up of Figure 7a shows how material from the lower layer is first entrained by the rising diapir and then gets dragged down by the return flow. Note the complex diapir shape at the end, with different dips for the margins depending on the structural level within the diapir and a small root zone below the main body.

[33] In a second calculation with the same large density contrast, we did not allow for brittle deformation (Figure 9). Once again, the initial stages are almost identical, and differences appear when the body reaches the level of the brittle-ductile transition. Without brittle deformation, the ascending body is blocked by the high viscosity of shallow crustal rocks. The laterally extensive upper surface of the diapir undergoes a Rayleigh-Taylor instability and adopts a

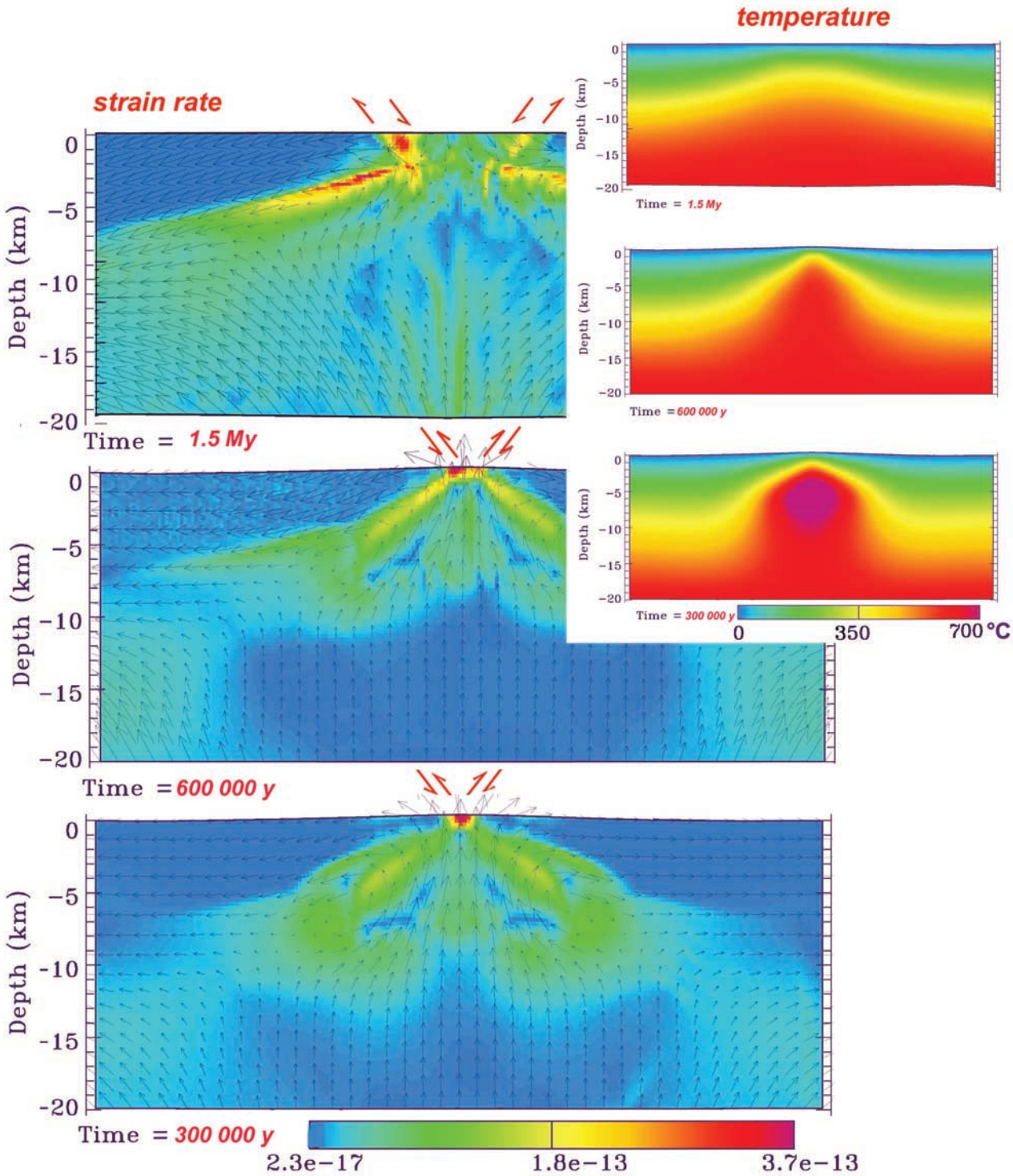

Figure 7b. Strain rate and temperature fields for the diapir of Figure 6. Faults develop in the uppermost crust when the local brittle strength is exceeded. Note that faulting occurs first in an inverse mode when the diapir is still far from its final emplacement depth and that it switches to a normal mode. When the diapir is at shallow depth, the temperature field develops a pointed structure due to the brittle ascent mechanism and is reminiscent of that for a spreading ridge.

different shape. Two bulges develop at the edges, and the central area experiences downsagging. It is worth to note that same erosion law was applied in both calculations. Hence it appears that erosion alone is not sufficient for near surface emplacement of magma bodies. Yet its role becomes crucially important when it is coupled with brittle deformation (Figure 9) [see also *Burov and Poliakov*, 2001].

4.3. Density Contrast

[34] In a series of calculations, we have used different values for the density contrast and have kept all other

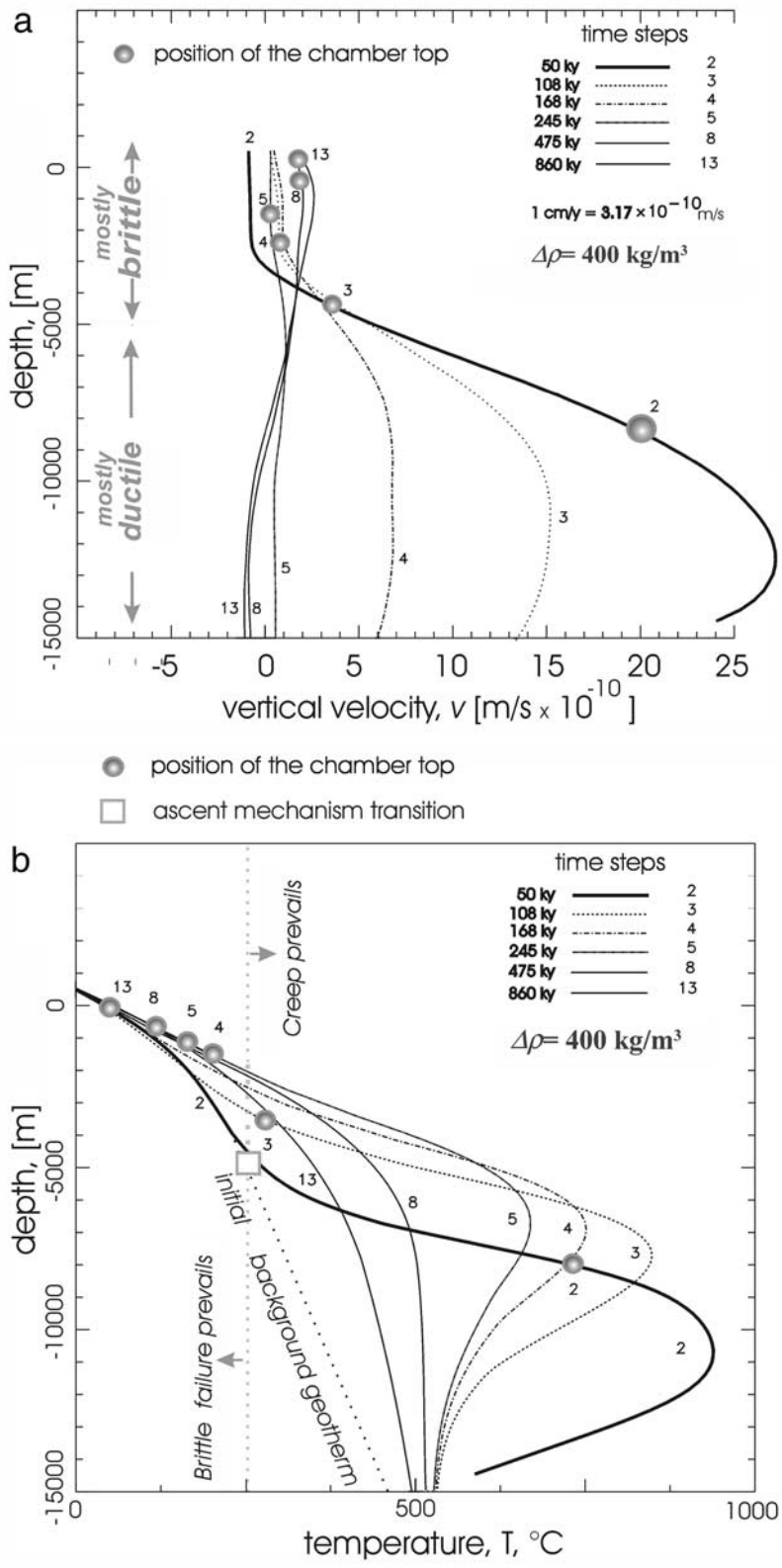

Figure 8. (a) Profiles of vertical velocity through the center of the diapir as a function of depth for the model of Figure 6. Solid circles indicate the top of the diapir. (b) Vertical temperature profiles through the diapir center as a function of depth for the model of Figure 6. Square indicates that brittle strength has been exceeded.

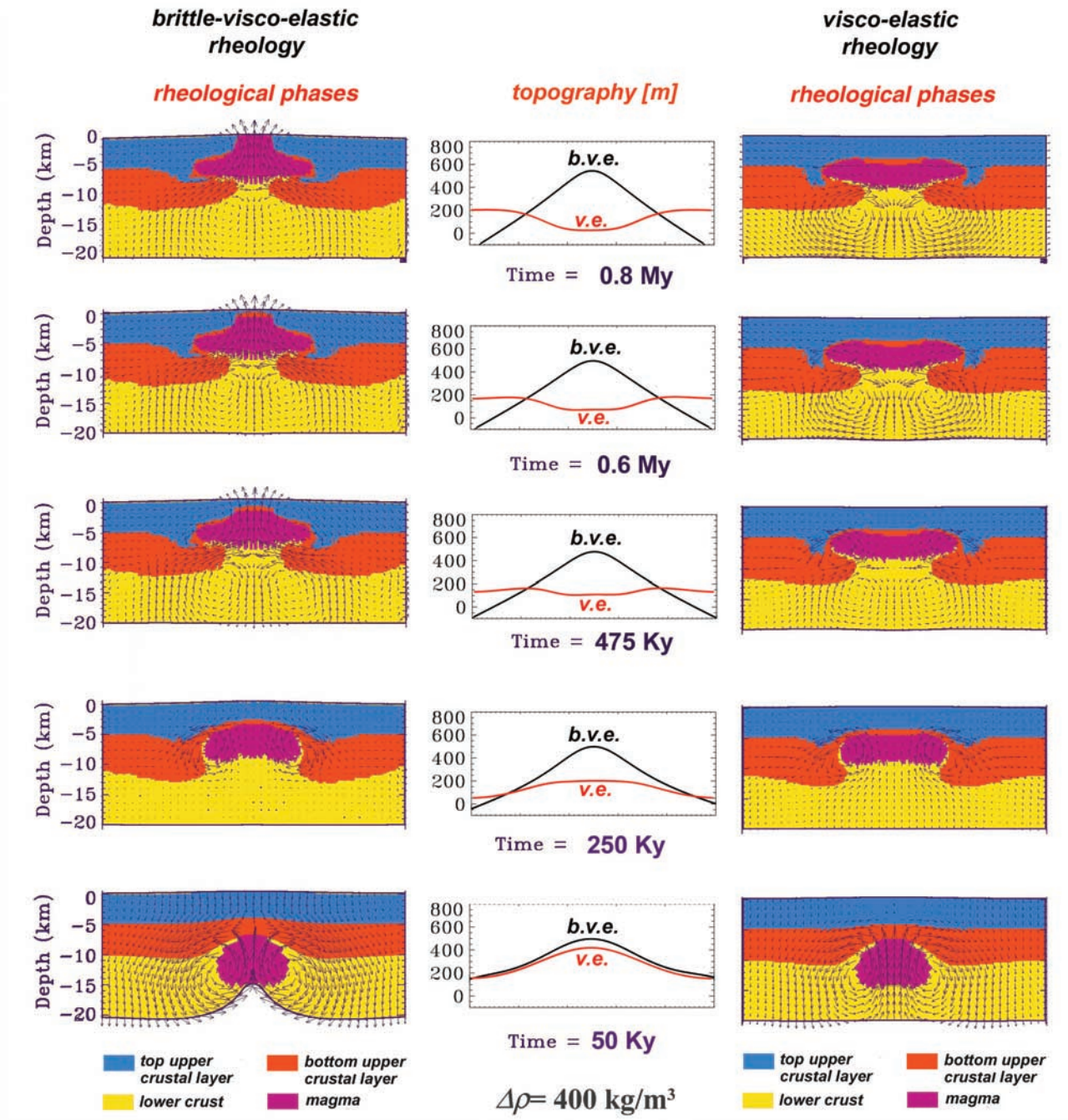

Figure 9. Comparison between two different assumptions for crustal deformation mechanisms. Calculations correspond to the diapir of Figure 6. (left) Brittle-elastic-ductile mechanisms (same as Figure 5). (right) Calculations with no brittle deformation (viscoelastic rheology). Note that the diapir flattens markedly and stops at a larger depth. The laterally extensive roof develops a Rayleigh-Taylor instability, with the dense uppermost crust collapsing into the diapir. This enhances flattening. (middle) Surface topography for the two models. The amplitude of anomalous topography is smaller for the model without brittle deformation. The "collapse" of roof rocks into the diapir is marked by a local depression at the center.

parameters at the same values. In all cases, the initial stages of ascent are quite similar to those of the reference case (Figure 10). However, for larger buoyancy, the ascent rate is larger. The thermal anomaly dissipates in the same amount of time, and hence allows ascent over a larger distance. As regards stresses above the reservoir, two effects reinforce one another and act to enhance brittle deformation: with increasing density contrast, buoyancy-induced stresses are larger and the final overburden thickness is smaller.

[35] Changing the bulk reservoir buoyancy therefore affects the final emplacement depth and the final emplacement mechanism. With increasing buoyancy, the final

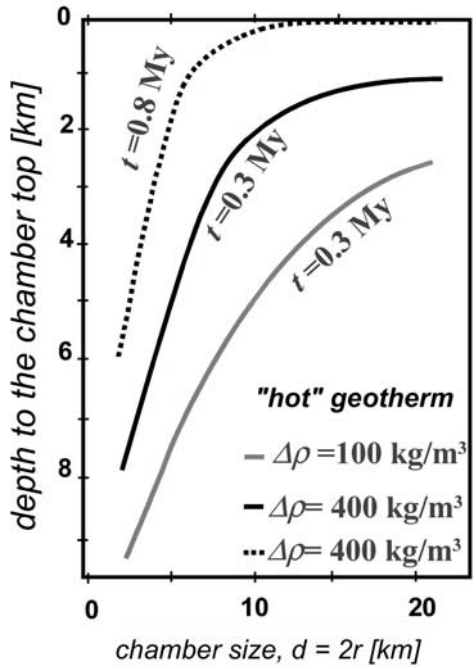

Figure 10. Depth to the chamber top at different times for different initial diapir sizes and density contrasts.

emplacement depth decreases. This also acts to activate faulting, and hence the buoyant body may ultimately reach the surface. For the present model, we found that brittle faulting requires reservoirs larger than about 7.5–10 km as well as large density contrasts.

4.4. Reservoir Size

[36] The reservoir size has a major effect on the results, because it determines the total buoyancy force involved, as well as the total amount of heat available for softening crustal rocks. It also determines which bodies may activate brittle faulting. Emplacement depth is a strong function of reservoir size (Figures 10 and 11).

4.5. Background Temperature Field

[37] Deformation of surrounding rocks depends on temperature and hence on the background thermal crustal structure. However, results for the hot and cold cases differ only slightly (Table 2 and Figure 11). The reason is that deformation gets focused in the thermal/ductile aureole around the ascending body, where temperatures and strain rates are much higher than background values and hence is not very sensitive to conditions in the far field.

5. Implications

5.1. Limitations of the Present Model

[38] Results have been obtained for a restricted range of parameters and crustal models and are summarized in schematic form in Figure 12. A single rheological law corresponding to ''dry quartz'' was used. It was not deemed useful to allow for other crustal rheologies because the results would change in a predictable manner. We have chosen to impose that, at the same temperature, the diapir material and surrounding rocks have the same strength. This is appropriate for the upper crust, but one may imagine different behaviors with surrounding rocks that have stronger or weaker rheology than the diapir. For detailed geological analysis, one should proceed on a case-by-case basis. For the sake of simplicity, we have not included latent heat and have ignored density changes due to crystallization and due to pressure dependence of the coefficient of thermal expansion. Thus it is not possible to discuss petrological issues in great detail.

[39] We have not included a far-field tectonic stress field. This would present no difficulty with the numerical code but would introduce yet another set of variables. It is clear that magmatic and plutonic activity occur in geologically active regions, and hence that one must discriminate between deformation due to the ascent of the magma body and superimposed regional deformation. We emphasize, however, that ascent proceeds even if the diapir is completely solid, which implies that solid-state deformation must not necessarily be attributed to tectonic stresses.

[40] It is worth emphasizing that the ignored effects (latent heat, crystallization, thermal expansion and regional extensional tectonic stress) would increase ascent rates and decrease the mechanical resistance of surrounding rocks, thus enhancing the emplacement mechanisms considered in this study.

5.2. Final Emplacement

[41] The calculations illustrate that emplacement depth may be controlled by temperature, through its effect on rheology. Indeed, many granitic plutons are associated with negative gravity anomalies, which demonstrates that they are not at a neutral buoyancy level and got stuck when they were still rising [e.g., *Guineberteau et al.*, 1987]. Here temperature does not refer to that of country rock in the far field but to the transient thermal evolution in a thin

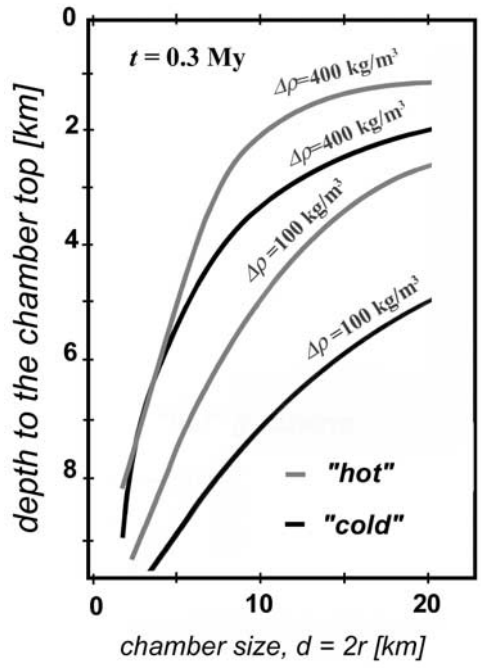

Figure 11. Depth to the chamber top at a time of 0.3 Myr for different initial diapir sizes, density contrasts, and two different background geotherms (see Table 2).

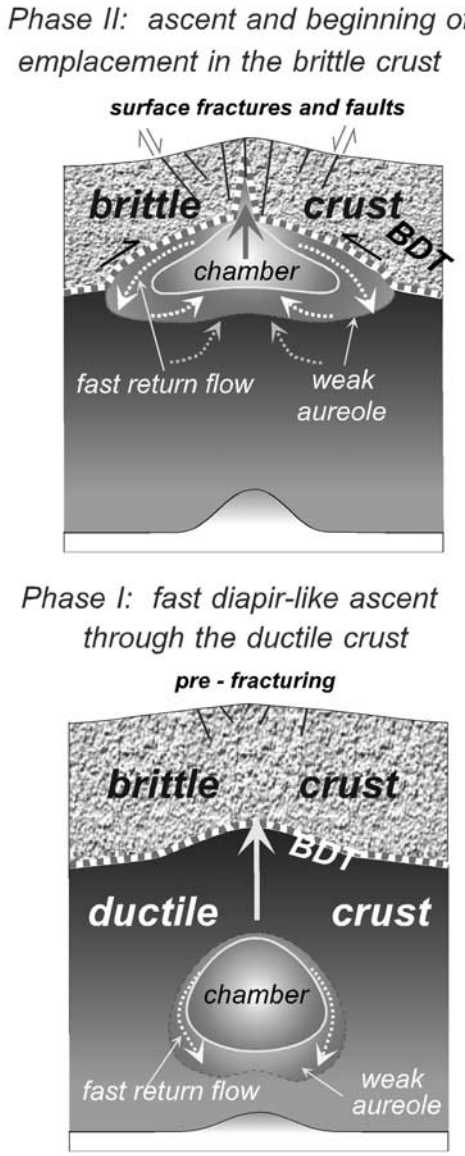

Figure 12. Summary of the various stages of diapir emplacement in the upper crust. Phase I is such that the diapir rises in a ductile regime with large velocities due to strain and thermal softening of surrounding rocks. In phase II, the diapir induces weakening and faulting at shallow levels and intrudes the uppermost crust.

aureole around the diapir. Thus emplacement depth cannot be determined by static considerations and must be solved for in a fully dynamic framework accounting for transient heat exchange between diapir and country rock, as has been attempted here. In reality, for given crustal structure and rheology, emplacement depth must be thought of as a function of diapir size and density anomaly. For such ''thermally controlled'' emplacement conditions, there are simple systematics. Only large plutons with diameters starting from 5 km are able to reach shallow crustal levels, and there is a relationship between pluton size and emplacement depth. Furthermore, the buoyant body flattens in a predictable way and there is a relationship between the final aspect ratio and the emplacement depth. Shallow emplacement conditions in the ductile regime involve horizontal spreading with little upward roof displacement (Figure 4).

[42] Plutons formed by dike injection should show different systematics. Here we restrict the discussion to flat plutons at relatively shallow crustal levels. There is strong evidence that laccoliths are fed from dikes and that they get emplaced in nearly neutral buoyant conditions, as shown by the lack of gravity anomalies over them [*Corry*, 1988]. In fact, dikes may overshoot the neutral buoyancy level [*Lister and Kerr*, 1990] and hence may even get quenched in surroundings that are less dense. Laccoliths clearly grow by upward displacement of overlying strata [*Corry*, 1988]. Such characteristics are different from those for thermally controlled emplacement. Consider for example tabular granites. These seldom exhibit uplifted roof rocks and are commonly associated with negative gravity anomalies [*Cruden*, 1998], features which are both compatible with the present model.

5.3. Brittle Faulting

[43] Except in extreme cases (large magma bodies and large density contrast), the ascent of a diapir involves little brittle faulting. Emplacement is thus achieved mostly in a ductile regime, however it occurs above the depth of the regional brittle-ductile transition, which is at least 10–15 km. This illustrates again the important fact that the brittle-ductile transition depends on local values of temperature and strain rate. Magma diapirs heat up their surroundings and hence augment the range of ductile behavior. Brittle faulting is most significant late in the ascent history when the body has already solidified and thus can apply important shear stresses on roof rocks (due to flattening), in addition to normal stresses due to buoyancy. This result is of course valid only for the assumptions and set of physical properties used in the calculations, but it is straightforward to evaluate the consequences for other choices. For example, country rocks with softer rheologies (''wet quartz'') would allow more rapid motion, less cooling during ascent, and hence shallower emplacement.

[44] Shallow emplacement involving brittle deformation is characterized by predominantly vertical motion at the top of the diapir (Figures 6 and 7). However, it is useful to note that there is also some ductile deformation at the base and hence that the relative importance of ductile and brittle deformation may vary with depth in the same unit.

5.4. Ballooning

[45] At shallow levels, deformation of host rocks in the ductile regime has little to do with ascent and is characterized by horizontal spreading. In this late phase, the chamber walls move laterally and hence lead to ballooning structures in host rocks. In this sense, ballooning may be seen as an inevitable consequence of emplacement near the surface (Figures 4 and 7). Here, ''near the surface'' means within about two initial diapir diameters from the surface. Thus, at depths in the range (5–20 km), one expects ballooning structures for plutons with diameters in the range of 5–10 km. Those conditions encompass most examples of geological relevance.

5.5. Caldera Resurgence and Peripheral Bulging

[46] The calculations emphasize that a buoyant body continues to rise when it has solidified. However, at such

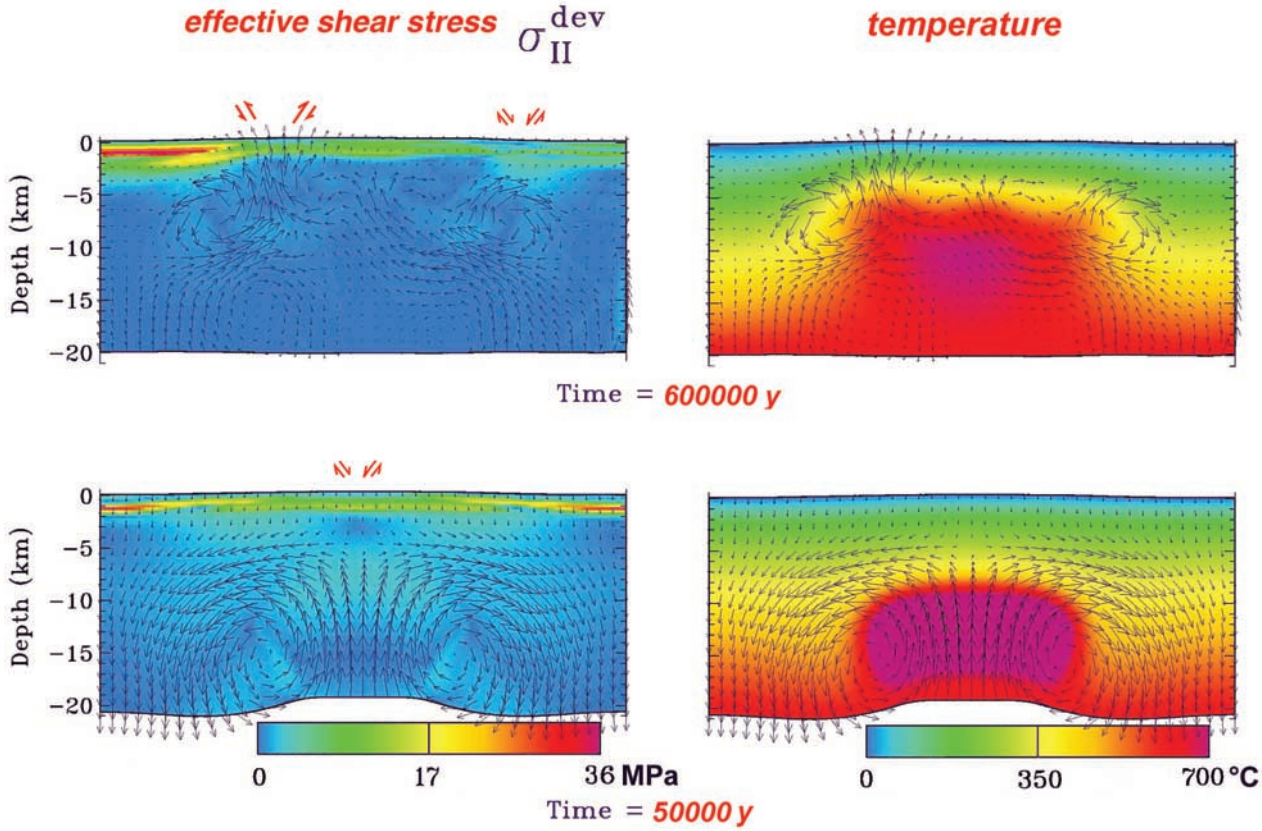

Figure 13a. Calculations for a very large diapir ($d \approx 20$ km), large density contrast ($\Delta\rho = 400$ kg m^{-3}) and a hot background geotherm. Rayleigh-Taylor instabilities develop on the roof region with three bulges growing upward and downsagging in between. Two zones of inverse faulting develop.

late stages, it cannot soften the surrounding rocks significantly, partly because of decreasing thermal energy and density contrast and partly due to colder and stiffer surrounding rock. Hence the ascent velocity becomes very much smaller than in the magmatic stage. According to our calculations, such a late phase may last for several hundred thousand years. A diapir with an initial diameter of 10 km, takes about 50 kyr to rise from 15–20 to 5 km in the ductile zone but another 50 kyr to rise from 5 to 4 km in the brittle-ductile zone (Figures 6 and 8). Smaller bodies would of course be even slower. In an ancient volcanic area, present-day deformation may therefore be associated with an extinct magmatic reservoir. Caldera resurgence [*Lipman*, 1984], which may be recorded several hundred thousand years after a climatic volcanic event, may be due to such late stage motion. In all cases, the experiments predict that a solidified magmatic body may keep some vertical motion for as much as 2 Myr. Naturally, there is no time limit for reactivation by external thermal or erosion events.

[47] In order to investigate large caldera systems, such as Yellowstone for example, we have carried out a calculation with a very large buoyant body with $d \approx 20$ km. Because of space limitations, it was not possible to start with an initially spherical shape and we have taken instead an ellipsoid (Figure 13a). This large volume flattens markedly as it rises. The upper interface extends over large horizontal distances and becomes unstable, with two peripheral bulges growing upward and downsagging in the central area

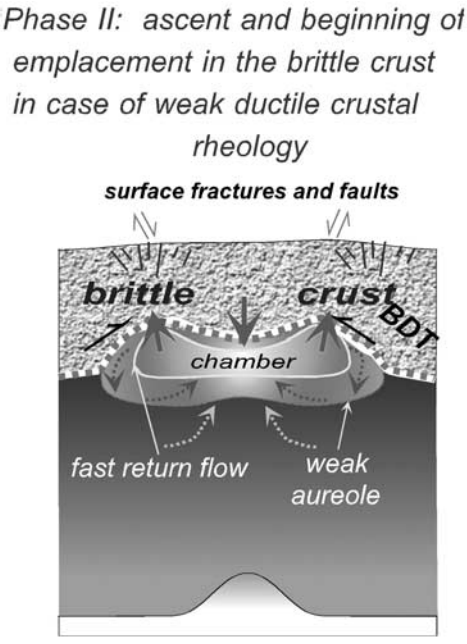

Figure 13b. Schematic diagram for the late stages of the previous calculation. Faulting has switched to the normal model and delineates a central depression. The middle bulge has been suppressed and only two peripheral bulges grow. There is downsagging in the central area.

(Figures 13a and 13b). This is strongly reminiscent of the present-day deformation pattern at Yellowstone, which is characterized by two resurgent domes and deflation elsewhere [*Dzurisin*, 2000]. It is clear that the situation at Yellowstone is more complicated than the relatively simple model developed here. However, gravity data do demonstrate that the caldera is underlain by low density material, which may well be silicic pluton [*Smith et al.*, 1974; *Lehman et al.*, 1982], and there is no reason to assume that this buoyant body remains completely immobile.

6. Conclusions

[48] We have reevaluated the dynamics of diapiric ascent in the upper crust using a thermomechanical model which allows for ductile and brittle deformation mechanisms as well as for deformation of the buoyant body.

[49] For thermally activated rheology, the final emplacement depth may be determined by the heat budget and a diapir may stall in dense country rock. Brittle behavior only becomes important at shallow crustal depths and hence is of no importance for diapirs which get emplaced at larger depths. The depth of emplacement is a decreasing function of diapir size and density anomaly. There are two different relationships between emplacement depth and diapir size, depending on the dominant late stage deformation mechanism (ductile or brittle). For typical diapir radii (5–10 km), predicted emplacement depths may be as shallow as a few kilometers depending on the density contrast. In all cases, surface erosion cannot be neglected but plays a relatively minor role.

[50] Diapir ascent rates in the "purely ductile" regime, between depths of about 30 and 10 km, may be as high as $0.1-5$ m yr^{-1}. In the "brittle-ductile" regime at shallower depth (about 10 to 5 km), ascent rates drop to values in the $0.01-0.05$ m yr^{-1} range. Finally, in the "brittle" regime, which is only important for diapirs which are able to rise within about 5 km of Earth's surface, ascent rates are still smaller and take typical values of a few millimeters per year. These estimates must be regarded as lower bounds because we have chosen to err on the conservative side (e.g., no latent heat, fixed thermal expansion, high rock cohesion, moderate erosion, no fluids, relatively low initial magma temperature and so on). The model calculations of this paper emphasize the importance of late stage motion at temperatures below magmatic values. Ascent and deformation may proceed for more than 1 Myr with a cold pluton.

[51] Ballooning characteristics may be generated by flattening. Predicted surface deformation features (topography, vertical and horizontal surface rates, stress and fault distribution) may help constrain the underlying magma reservoir geometry, as well as its emplacement dynamics.

Appendix A: Numerical Model

[52] The "2.5-D" numerical scheme is a modified version of the PAROVOZ code [*Poliakov et al.*, 1993a] based on the FLAC algorithm [*Cundall*, 1989]. This code operates on a 2-D Cartesian frame but all internal stress-strain relations are solved in full 3-D formulation, which allows to account for out-of-plane components. The code is a dynamic fully explicit time-marching large-strain Lagrangian algorithm that solves the full Newtonian equations of motion:

$$\rho\frac{\partial}{\partial t}\left(\frac{\partial \mathbf{u}}{\partial t}\right) - \mathrm{div}\sigma - \rho\mathbf{g} = 0 \tag{A1}$$

coupled with constitutive equations of kind:

$$\frac{D\sigma}{Dt} = F\left(\sigma, \mathbf{u}, \nabla\frac{\partial \mathbf{u}}{\partial t}, \ldots T \ldots\right) \tag{A2}$$

and with those of heat transfer (diffusion and advection):

$$\rho C_p \partial T/\partial t + \dot{\mathbf{u}}\nabla T - \mathrm{div}(k\nabla T) - H_r = 0 \tag{A3}$$

and surface erosion (linear or nonlinear diffusion):

$$\partial h_s/\partial t - \nabla(k_e \nabla h_s) = 0, \tag{A4}$$

where $\mathbf{u}$, $\dot{\mathbf{u}}$, σ, $\mathbf{g}$ are the respective vector-matrix terms for the displacement, displacement velocity, stress, acceleration due body forces, and thermal conductivity; t, ρ, C_p, T, k, H_r, h_s, and k_e denote time, density, specific heat, temperature, thermal conductivity, internal heat production, surface elevation and coefficient of erosion, respectively. The terms $\partial/\partial t$, D/Dt, and F denote a time derivative, an objective time derivative, and a functional, respectively.

[53] The numerical scheme provides velocities at mesh points, which permit to calculate element strains. These strains are used in the constitutive relations to calculate element stresses and equivalent forces, which form the basic input for the next calculation cycle. The Lagrangian coordinate mesh moves with the material, and at each time step the new positions of the mesh grid nodes are calculated and updated in large strain mode from the current velocity field using an explicit procedure (two-stage Runge-Kutta). To solve explicitly the governing equations, the Parovoz (FLAC) method uses a dynamic relaxation technique by introducing artificial masses in the inertial system. Adaptive remeshing technique developed by A. N. B. Poliakov and Y. Podladchikov [*Poliakov et al.*, 1993a, 1993b] permits to resolve strain localizations leading to formation of the faults. The solver of the FLAC method does not imply any inherent rheology assumptions, in contrast with the most common finite element techniques based on the implicit displacement method. The main interest in this method thus refers to its capability to model physically highly unstable processes and handle strongly nonlinear rock rheologies in their explicit form of the constitutive relationship between strain and stress.

A1. Explicit Plastic-Elastic-Viscous Rheology

[54] In contrast to conventional fluid dynamic approaches, where nonviscous terms such as plastic (brittle) and elastic terms are replaced with pseudoplastic and pseudoelastic viscous rheology terms, the present method treats these terms in explicit way. The elastic-ductile-plastic rheology chosen for crust and diapir is derived from rocks mechanics data. Mohr-Coulomb plasticity, elastic and viscous (linear or nonlinear) terms are introduced explicitly, in a way that any element in the mesh has the potential for elastic, viscous, and plastic deformation. The total strain

increments in each numeric element are defined by a sum of elastic, viscous and brittle strain increments. The corresponding constitutive behavior is schematically represented as usual serial connection of an elastic spring, of a viscous dashpot and of a plastic frictional block [e.g., *Cundall*, 1989].

A2. Plastic (Brittle) Behavior

[55] The brittle behavior of the uppermost lithosphere is given by experimentally derived *Byerlee*'s [1978] law, which describes time-independent discontinuous frictional slip on a pervasively fractured rock volume:

$$\tau \approx 0.85\sigma_n, \quad \sigma_n \leq 200\,\mathrm{MPa} \tag{A5}$$

$$\tau \approx 0.5\,\mathrm{MPa} + 0.6\sigma_n, \quad \sigma_n > 200\,\mathrm{MPa} \tag{A6}$$

or

$$\sigma_1 - \sigma_3 \approx 4\sigma_3, \quad \sigma_3 \leq 110\,\mathrm{MPa} \tag{A7}$$

$$\sigma_1 - \sigma_3 \approx 2.1\sigma_3 + 210\mathrm{MPa}, \quad \sigma_3 > 110\mathrm{MPa}, \tag{A8}$$

where τ is shear stress and σ_n is effective normal stress, σ_1 and σ_3 are principal stresses. Byerlee's law matches a pressure-dependent Mohr-Coulomb material with friction angle ϕ and cohesion $|C_0|$ [e.g., *Gerbault et al.*, 1998]:

$$|\tau| = C_0 - \tan\phi\sigma_n, \tag{A9}$$

where σ_n is normal stress $\sigma_n = P + \sigma_{\mathrm{II}}^{\mathrm{dev}} \sin\phi$, P is the effective pressure, $\sigma_{\mathrm{II}}^{\mathrm{dev}}$ is the second invariant of the deviatoric stress, or effective shear stress. Condition of transition to brittle deformation (function of rupture f) reads as: $f = \sigma_{\mathrm{II}}^{\mathrm{dev}} + P \sin\phi - C_0 \cos\phi = 0$ and $\partial f/\partial t = 0$. In terms of principal stresses, the equivalent of the yield criterion reads as

$$\sigma_1 - \sigma_3 = -\sin\phi\left(\sigma_1 + \sigma_3 - 2C_0 \tan^{-1}\phi\right). \tag{A10}$$

Parameters $\phi = 30°–33°$ and $|C_0| = 5–20$ MPa represent Byerlee's law for most rocks. In case of important fluid pressure, σ_n is reduced to $\sigma_n' = \sigma_n - P_f$, where P_f is fluid pressure.

A3. Elastic Behavior

[56] The elastic part is defined using commonly inferred values of elastic constants for lithospheric rocks, that is with Young modulus, E, of 75 GPa and Poisson's ratio, υ, of 0.25 [e.g., *Turcotte and Schubert*, 1982]:

$$\sigma_{ik} = (\lambda + 2\mu 3^{-1})\varepsilon_{ll}\delta_{ik} + 2\mu\left(\varepsilon_{ik} - 3^{-1}\varepsilon_{ll}\delta_{ik}\right), \tag{A11}$$

where λ and μ are Lamé's constants (Table 2) related to E and υ as $\lambda = E\upsilon\,[(1+\upsilon)(1-2\upsilon)]^{-1}$; $\mu = E(2(1+\upsilon))^{-1}$, δ is Kronecker's delta.

A4. Viscous (Ductile Creep) Behavior

[57] A non-Newtonian ductile rheology [e.g., *Kohlstedt et al.*, 1995] is presented by power law stress and exponential temperature dependence of the strain rate:

$$\dot{\varepsilon}_{ij} = A\sigma_{\mathrm{II}}^{\mathrm{dev}}\sigma_{ij}^{n-1} \exp(-Q/RT), \tag{A12}$$

where $\dot{\varepsilon}$ is the strain rate, $\sigma_{\mathrm{II}}^{\mathrm{dev}} = 0.5(\sigma_{ij}\sigma_{ij})^{1/2}$ is the effective stress (second invariant of the deviatoric stress σ), A is the material parameter, n is the effective stress exponent, Q is the creep activation energy, T is the absolute temperature, and R is the universal gaz constant. The variables A, n, Q describe the properties of a specific material (Table 2). Creep deformation is strongly different from that of constant viscosity or temperature-dependent Newtonian fluid because the effective viscosity of a power law material may vary within 10 orders of magnitude as a function of the deviatoric stress even at adiabatic temperature conditions.

A5. Brittle-Ductile Interactions

[58] The ductile-elasto-brittle rheology used here is represented as a serial connection of an elastic string component, frictional block component and a nonlinear viscous dashpot component. The total incremental strain in such a system is a sum of incremental viscous, plastic and elastic strains in each of the components, whereas the steady state component stresses are equal. On each time step, the algorithm uses current solution for strain and strain rate in each numerical element to predict potential incremental stress in each of the three rheological components for the next time step. The component which predicts lowest stress for given strain effectively dominates the overall behavior of the grid element. Exact constitutive relations for each component are solved on each time step, which makes the algorithm very robust. The behavior of each rheological component plugged in a chain may be completely different from its stand-alone behavior. For example, pure viscous deformation does not depend on strain, but in elastoviscous material, the initial strain controls the viscous stress and strain rate. In a serial viscoplastic medium, the plastic stress limits the viscous stress (and vice versa), and consequently the viscous strain rate. Thus a plastic component, which is alone strain rate-independent, controls, and is being controlled by, the strain rate in a viscoplastic couple. For this reason, in the vicinity of the brittle-ductile transition, the velocity field in both ductile and brittle zones is controlled by the behavior of all, ductile, brittle, and elastic parts. This behavior is difficult to reduce to that of a simple single-phase or biphase material such as viscous, viscoelastic, or plastoelastic.

A6. Free Surface Boundary Condition

[59] The code handles explicit free surface boundary condition. Thus different from a number of existing codes, the surface velocity and displacement are computed in a straightforward way, without simplifying assumptions.

A7. Surface Erosion and Sedimentation

[60] Linear or nonlinear diffusion equation (A4) well represent so-called short-range surface processes associated with small scale topography elevations [e.g., *Avouac and Burov*, 1996; *Burov and Cloetingh*, 1997]. In particular, the

diffusion equation assures a number of important properties of the surface processes: (1) dependence of the local erosion rate on surface curvature and slope, so that actively deforming topography is subject to faster erosion; (2) mass conservation; and (3) smoothing of the surface with time in the absence of active subsurface deformation.

[61] **Acknowledgments.** The version of the code PAROVOZ used is this study was derived from original source code developed during 1991–1997 by A. Poliakov in association with Y. Podladchikov, who are deeply thanked for their generous help and availability. We especially thank S. Paterson for many useful comments on the manuscript. J.-P. Milesi and C. Fouillac are deeply thanked for their encouragement and support. This is BRGM contribution 02107. This study was supproted by IT program of INSU.

References

Avouac, J.-P., and E. B. Burov, Erosion as a driving mechanism of intracontinental mountain growth?, *J. Geophys. Res.*, *101*, 17,747–17,769, 1996.

Batchelor, G. K., *An Introduction to Fluid Dynamics*, 615 pp., Cambridge Univ. Press, New York, 1967.

Bateman, R., On the role of diapirism in the segregation, ascent and final emplacement of granitoid magmas, *Tectonophysics*, *110*, 211–231, 1984.

Bateman, R., Progressive crystallization of a granitoid diapir and its relationship to stages of emplacement, *J. Geol.*, *93*, 645–662, 1985.

Bills, B. G., D. Currey, and G. A. Marshall, Viscosity estimates for the crust and upper mantle from patterns of lacustrine shoreline deformation in the eastern Great Basin, *J. Geophys. Res.*, *99*, 20,259–20,286, 1994.

Bittner, D., and H. Schmeling, Numerical modelling of melting processes and induced diapirism in the lower crust, *Geophys. J. Int.*, *123*, 59–70, 1995.

Bos, B., and C. J. Spiers, Frictional-viscous flow in phyllosilicate-bearing fault rock: Microphysical model and implications for crustal strength profiles, *J. Geophys. Res.*, *107*(B2), 2028, doi:10.1029/2001JB000301, 2002.

Brace, W. F., and D. L. Kohlstedt, Limits on lithospheric stress imposed by laboratory experiments, *J. Geophys. Res.*, *85*, 6248–6252, 1980.

Burov, E. B., and S. Cloetingh, Erosion and rift dynamics: New thermomechanical aspects of post-rift evolution of extensional basins, *Earth Planet Sci. Lett.*, *150*, 7–26, 1997.

Burov, E. B., and M. Diament, Flexure of the continental lithosphere with multilayered rheology, *Geophys. J.*, *109*, 449–468, 1992.

Burov, E. B., and L. Guillou-Frottier, Thermomechanical behavior of large ash flow calderas, *J. Geophys. Res.*, *104*, 23,081–23,109, 1999.

Burov, E., and A. Poliakov, Erosion and rheology controls on synrift and postrift evolution: Verifying old and new ideas using a fully coupled numerical model, *J. Geophys. Res.*, *106*, 16,461–16,481, 2001.

Byerlee, J. D., Friction of rocks, *Pure Appl. Geophys.*, *116*, 615–626, 1978.

Carmichael, R. S., *Physical Properties of Rocks and Minerals*, 741 pp., CRC Press, Boca Raton, Fla., 1989.

Carter, N. L., and M. C. Tsenn, Flow properties of continental lithosphere, *Tectonophysics*, *36*, 27–63, 1987.

Chéry, J., A. Bonneville, J.-P. Vilotte, and D. Yuen, Numerical modeling of caldera dynamical behavior, *Geophys. J. Int.*, *105*, 365–379, 1991.

Chester, F. M., A rheologic model for wet crust applied to strike-slip faults, *J. Geophys. Res.*, *100*, 13,033–13,044, 1995.

Clemens, J. D., Observations on the origins and ascent mechanisms of granitic magmas, *J. Geol. Soc. London*, *155*, 845–851, 1998.

Corry, C. E., Laccoliths: Mechanics of emplacement and growth, *Spec. Pap. Geol. Soc. Am.*, *220*, 110 pp., 1988.

Cruden, A. R., Deformation around a rising diapir modeled by creeping flow past a sphere, *Tectonics*, *7*, 1091–1101, 1988.

Cruden, A. R., On the emplacement of tabular granites, *J. Geol. Soc. London*, *155*, 853–862, 1998.

Cundall, P. A., Numerical experiments on localization in frictional materials, *Ing. Arch.*, *59*, 148–159, 1989.

Dzurisin, D., Volcano geodesy: Challenges and opportunities for the 21st century, *Philos. Trans. R. Soc. London, Ser. A*, *358*, 1547–1566, 2000.

Gerbault, M., A. Poliakov, and M. Daignières, Prediction of faulting from the theories of elasticity and plasticity: What are the limits?, *J. Struct. Geol.*, *20*, 301–320, 1998.

Guillou-Frottier, L., E. B. Burov, and J.-P. Milesi, Genetic links between ash-flow calderas and associated ore deposits as revealed by large-scale thermo-mechanical modeling, *J. Volcanol. Geotherm. Res.*, *102*, 339–361, 2000.

Guineberteau, B., J. Bouchez, and J. Vigneresse, The Mortange granite pluton (France) emplaced by pull-apart along a shear zone: Structural and gramimetric arguments and regional implications, *Geol. Soc. Am. Bull.*, *99*, 763–770, 1987.

Happel, J., and H. Brenner, *Low Reynolds Number Hydrodynamics*, 553 pp., M. Nijhoff, Dordrecht, 1983.

Judd, W. R., and A. Shakoor, Density, in *Physical Properties of Rocks and Minerals*, edited by Y. S. Touloukian, W. R. Judd, and R. F. Roy, pp. 29–43, McGraw-Hill, New York, 1981.

Kirby, S. H., and S. H. Kronenberg, Correction to "Rheology of the lithosphere: Selected topics," *25*, 1680–1681, 1987.

Kohlstedt, D. L., B. Evans, and S. J. Mackwell, Strength of the lithosphere: Constraints imposed by laboratory experiments, *J. Geophys. Res.*, *100*, 17,587–17,602, 1995.

Lehman, J. A., R. B. Smith, M. M. Schilly, and L. W. Braile, Upper crustal structure of the Yellowstone caldera from delay time analyses and gravity correlations, *J. Geophys. Res.*, *87*, 2713–2730, 1982.

Lipman, P. W., The roots of ash-flow calderas in western North America: Windows into the tops of granitic batholiths, *J. Geophys. Res.*, *89*, 8801–8841, 1984.

Lister, J. R., and R. C. Kerr, Fluid-mechanical models of dyke propagation and magma transport, in *Mafic Dykes and Emplacement Mechanisms*, edited by A. J. Parker, P. C. Rickwood, and D. H. Tucker, pp. 69–80, A. A. Balkema, Brookfield, Vt., 1990.

Mahon, K. I. T., M. Harrison, and D. A. Drew, Ascent of a granitoid diapir in a temperature varying medium, *J. Geophys. Res.*, *93*, 1174–1188, 1998.

Miller, R. B., and S. R. Paterson, The transition from magmatic to high-temperature solid-state deformation: Implications from the Mount Stuart batholith, Washington, *J. Struct. Geol.*, *16*, 853–865, 1994.

Miller, R. B., and S. R. Paterson, In defense of magmatic diapirs, *J. Struct. Geol.*, *21*, 1161–1173, 1999.

Molyneux, S. J., and D. H. W. Hutton, Evidence for significant granite space creation by the ballooning mechanism: The example of the Ardara pluton, Ireland, *Geol. Soc. Am. Bull.*, *112*, 1543–1558, 2000.

Paterson, S. R., and T. K. Fowler Jr., Reexamining pluton emplacement mechanisms, *J. Struct. Geol.*, *15*, 191–206, 1993.

Petford, N., R. C. Kerr, and J. R. Lister, Dike transport of granitoid magmas, *Geology*, *21*, 845–848, 1993.

Petford, N., A. R. Cruden, K. J. W. McCaffrey, and J.-L. Vigneresse, Granite magma formation transport and emplacement in the Earth's crust, *Nature*, *408*, 669–673, 2000.

Poliakov, A. N. B., P. Cundall, Y. Podlachikov, and V. Laykhovsky, An explicit inertial method for the simulation of visco-elastic flow: An evaluation of elastic effects on diapiric flow in two- and three-layers models, in *Flow and Creep in the Solar System: Observations, Modeling and Theory*, *NATO ASI Ser., Ser. E*, vol. 391, edited by D. B. Stone and S. K. Runcorn, pp. 175–195, Kluwer Acad., Norwell, Mass., 1993a.

Poliakov, A. N. B., Y. Podladchikov, and C. Talbot, Initiation of salt diapirs with frictional overburden: Numerical experiments, *Tectonophysics*, *228*, 199–210, 1993b.

Roman-Berdiel, T., D. Gapais, and J.-P. Brun, Analogue models of laccolith formation, *J. Struct. Geol.*, *17*, 1337–1346, 1995.

Rubin, A. M., Dykes vs diapirs in viscoelastic rock, *Earth Planet Sci. Lett.*, *117*, 653–670, 1993.

Schmeling, H., A. R. Cruden, and G. Marquart, Finite deformation in and around a sphere moving through a viscous medium: Implications for diapiric ascent, *Tectonophysics*, *149*, 17–34, 1988.

Smith, R. B., R. T. Shuey, J. R. Pelton, and J. P. Bailey, Yellowstone hot spot: New magnetic and seismic evidence, *Geology*, *2*, 451–455, 1974.

Turcotte, D., and G. Schubert, *Geodynamics: Applications of Continuum Physics to Geological Problems*, 2nd ed., 456 pp., Cambridge Univ. Press, New York, 2002.

Weinberg, R. F., and Y. Podladchikov, Diapiric ascent of magmas through power law crust and mantle, *J. Geophys. Res.*, *99*, 9543–9559, 1994.

E. Burov, Laboratoire de Tectonique UMR 7072, Université Pierre et Marie Curie, 4 Place Jussieu, 75252 Paris cedex 05, France. (evgenii.burov@lgs.jussieu.fr)

L. Guillou-Frottier, Bureau des Recherches Géologiques et Minières, REM, 3, av. C. Guillemin, BP6009, F-45060 Orléans cedex 2, France. (l.guillou-frottier@brgm.fr)

C. Jaupart, Institut de Physique du Globe de Paris, 4 Place Jussieu, 75252 Paris cedex 05, France. (cj@ccr.jussieu.fr)